Imaging heterogeneous absorption distribution of advanced breast cancer by optical tomography

Yan Xu
Quing Zhu
University of Connecticut
Department of Electrical and Computer Engineering
Storrs, Connecticut 06269

Abstract. Tumor vascular patterns of advanced breast cancers are complex and heterogeneous. Two typical light absorption patterns of periphery enhancement and posterior shadowing have been observed when imaging these advanced cancers using optical tomography guided by ultrasound. We perform a series simulation and phantom experiments to systemically evaluate the effects of target parameters, target locations, and target optical properties on imaging periphery enhancement absorption distribution using reflection geometry. Large tumors are modeled as concentric semiellipsoidal targets of different outer shell and inner core optical properties. We show that larger targets of more than 3 to 4 cm diameter with outer shell thicknesses less than 1 cm can be resolved at a depth less than 3 cm. A clinical example is given to show the complex vasculature distributions seen from an advanced cancer.
 [DOI: 10.1117/1.3505015]

Keywords: diffused light propagation; Monte Carlo method; advanced breast cancer imaging; optical tomography.

Paper 10265RR received May 17, 2010; revised manuscript received Sep. 2, 2010; accepted for publication Sep. 10, 2010; published online Dec. 8, 2010.

1 Introduction

Optical tomography has tremendous potential to provide clinically useful functional information about tumor angiogenesis and tumor hypoxia.[1–22] However, the process of tumor angiogenesis is complex, resulting in a highly distorted and heterogeneous distribution of blood vessels in advanced cancers.[23] This distorted distribution is dependent on angiogenic factors and related to the incorporation of existing host blood vessels into tumor and the creation of new tumor microvessels.[24,25] The distribution of these tumor vessels is highly heterogeneous. Some areas may have a high microvessel density, especially in the periphery of the tumor; other areas may develop necrosis, especially in the central region of the tumor.[26,27] In our pilot studies of imaging tumor vasculature using ultrasound (US) guided optical tomography, we observed heterogeneous absorption distribution in advanced cancers.[19,22,28] In this paper, we systemically investigate the capability of optical tomography to accurately image heterogeneous absorption distributions using Monte Carlo simulations and phantom experiments. A clinical example is given to show the complex vasculature distributions seen from an advanced cancer. To the best of our knowledge, this study is the first one to characterize and quantify the effects of target parameters, target locations, and target optical properties on imaging heterogeneous absorption distributions of large targets in reflection geometry. Understanding and characterizing the features of advanced breast cancers imaged by optical tomography is a critical step toward translating this promising technique into clinical practice. It is also important to understand the initial angiogenesis distributions and potential angiogenesis changes of advanced cancers when patients have undergone neoadjuvant chemotherapy.

2 Methods

2.1 *Monte Carlo Simulation*

The time-domain Monte Carlo (MC) method was used to generate the forward data with a target inside the turbid medium located at different depths. The details of the time-domain MC simulation developed by our group can be found in Ref. 29 and 30. Briefly, the reflection geometry with multiple sources and detectors distributed on a probe of 10 cm diameter was used in the MC simulation (see Fig. 1). At each source location, a delta pulse consisting of 30 millions photons was lunched into the medium. Initially, each photon was assigned a unity weight W, which is analogous to light intensity. Each photon went through many steps of absorption and scattering processes. After each step, a part of the weight ΔW was absorbed by the medium and the weight of the photon was decreased. The photon was scattered following the Henyey-Greenstein function. The roulette technique was used to terminate the photon when the residual weight was less than a threshold value. For each photon, it was either absorbed in the medium, detected at the reflecting surface, or left from the transmitting surface. After the migration of one particular photon halted, a new photon was launched into the medium at the source location. In this simulation, the absorption boundary was used between the scattering medium and the outer surface. Each photon's energy and arrival time were recorded when the photon reached the outer surface (boundary). The distribution or time profile of the recorded photons at each detector position for each delta pulse at a source position was stored and the resulting temporal data were Fourier transformed to provide

Address all correspondence to: Quing Zhu, Department of Electrical and Computer Engineering, University of Connecticut, 371 Fairfield Rd., 41157, Storrs, CT 06269. Tel: 860-486-5523; Fax: 860-486-2447; E-mail: zhu@engr.uconn.edu.

1083-3668/2010/15(6)/066007/17/$25.00 © 2010 SPIE

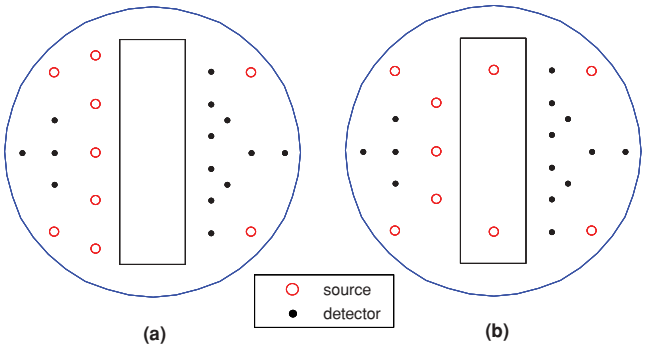

Fig. 1 Probe geometry used for simulation and phantom experiments (a) without and (b) with closer-to-center center sources.

frequency domain amplitude and phase shift at 140 MHz, which was used in simulations.

The MC program was extended to include a larger semiellipsoidal inhomogeneous target embedded inside a turbid medium, which closely models large breast lesions when patients are imaged in a supine position using the conventional pulse-echo US and our handheld combined probe. In addition, most of the large lesions are squashed into a semiellipsoidal shape against the chest wall under the slight probe compression. Therefore, a semiellipsoidal target is a reasonable model for these lesions. As shown in Fig. 2(a), the inhomogeneous target has two concentric semiellipsoids of different outer shell and inner core optical properties. The boundary conditions between target layers and medium could be easily controlled by mapping corresponding refractive indexes in an input file.

When a photon propagated to one of the boundaries between the target outer layer and the medium, the target outer layer and the core or the target core and the medium, the intersection point [point P in Fig. 2(a)] was computed and the shortened step size (s_1) of this photon from B to P was calculated. At the incident angle ($\angle NPB$), Snell's law was applied to calculate the reflection angle ($\angle NPC$) and the refraction angle ($\angle MPD$). After this photon traveled a distance s_1, the traveling direction was changed, depending on different boundary conditions. If the photon experienced total internal reflection, the photon was propagated in the same medium with the reflection direction. If the photon experienced partial internal reflection, one simplification was made by assuming the photon would be either all reflected or all refracted. By comparing the reflection coefficient from Fresnel's equations and a random number generated from a uniform distribution, the photon would be refracted only if the random number was larger than the reflection coefficient; otherwise, it would be reflected. Thus, the remaining step size (s_2) of the photon was propagated in the corresponding medium determined above. As the photon propagated in the medium, part

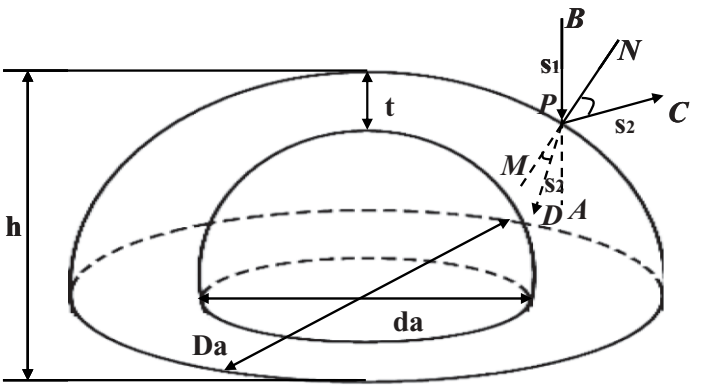

(a)

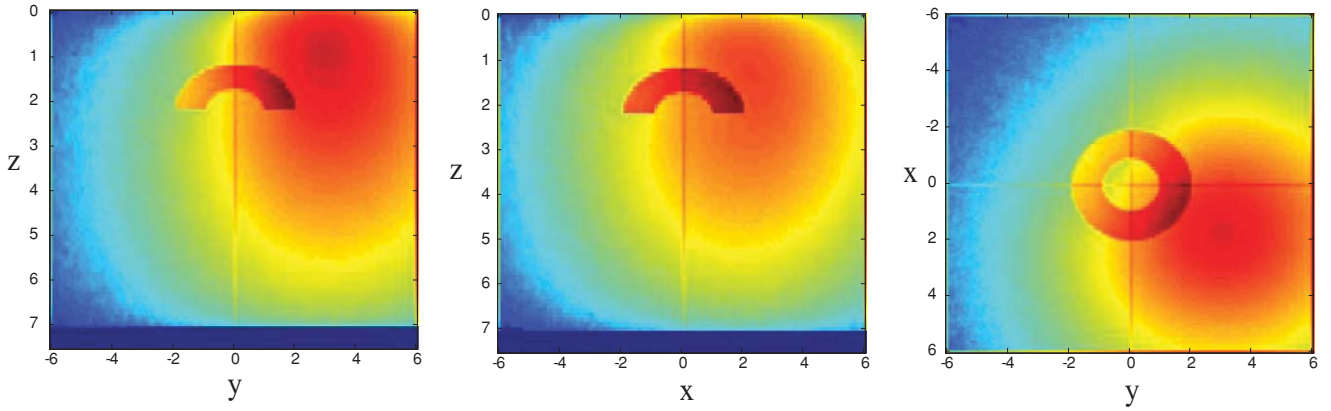

(b)

Fig. 2 (a) Geometry of the photon propagation to the boundary of a concentric semi-ellipsoidal target and (b) ΔW inside the 3-D volume summed in the x direction (left), the y direction (middle), and the z direction (right), respectively, and projected into the y-z plane, the x-z plane, and the x-y plane, respectively.

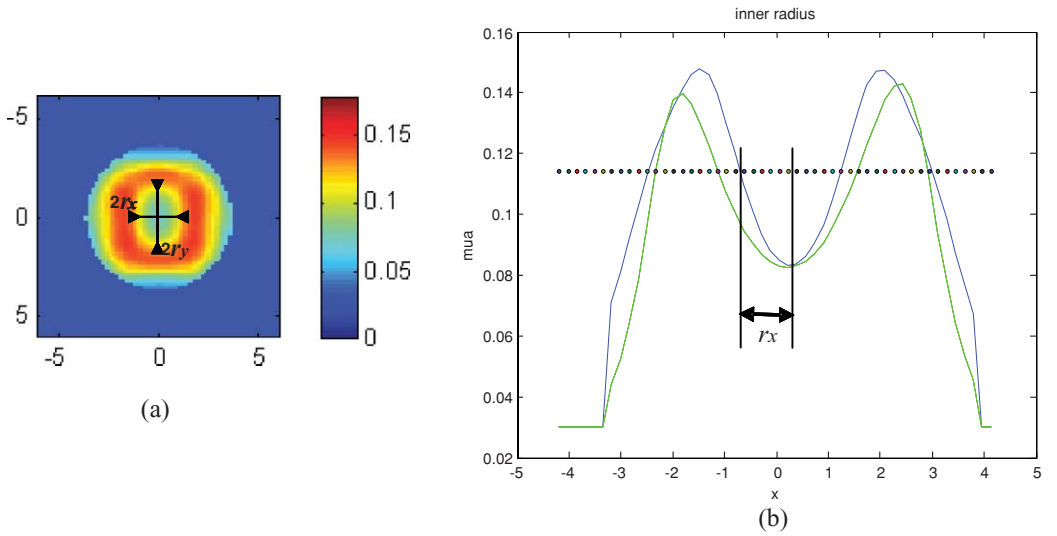

Fig. 3 Illustration of measuring reconstructed inner radius.

of the weight ΔW was absorbed after each step. The absorbed ΔW inside the 3-D volume was summed in the x direction, the y direction, and the z direction, respectively, and projected into the y-z plane, the x-z plane, and the x-y plane, respectively, as shown in Fig. 2(b).

2.2 *Imaging Reconstruction*

The Born method was used to approximate the received photon density wave as a linear superposition of homogeneous incident and scattered fields originated from a source located at r_s and evaluated inside the medium at r:

$$U(r_s, r) = U_0(r_s, r) + U_{\mathrm{SC}}(r_s, r). \tag{1}$$

Under the approximation that $U_0(r_s, r) \gg U_{\mathrm{SC}}(r_s, r)$, U_{SC} could be derived as

$$U_{\mathrm{SC}}(r_s, r_d) = -1/D_0 \int G(r - r_d)\Delta\mu_a(r)U_0(r_s, r)\,\mathrm{d}^3 r, \tag{2}$$

where $G(r - r_d)$ is the Green's function, which relates the scattered field measured at the detector r_d to the field point r; $\Delta\mu_a(r)$ represents the absorption variation at the voxel r; and D_0 is the diffusion coefficient of the homogenous medium.

The dual-zone mesh scheme introduced by us earlier was used for inversion.[31] Briefly, the imaging volume was segmented into two regions consisting of the lesion [region of interest (ROI)] as identified by the coregistered US and the background region. We used a smaller fine mesh size for the lesion region and a larger coarse mesh size for the background region, so that the total voxels with unknown optical properties was significantly reduced and the inversion converged quickly in three to four iterations. The conjugate gradient method was used for the iterative optimization.

Typically, in simulations and phantom experiments, the fine mesh region was chosen about 3 to 4 times larger than the true target area, and in clinical data, the fine mesh region was about 4.5 times larger than the lesion area estimated by US. Using this dual-zone mesh method, the scattered field can be related to the total absorption distribution as:

$$[U_{\mathrm{SC}}]_{M\times 1} = [\boldsymbol{W}_L, \boldsymbol{W}_B]_{M\times N}[\boldsymbol{M}_L, \boldsymbol{M}_B]^T, \tag{3}$$

where $\boldsymbol{W}_L$ and $\boldsymbol{W}_B$ are the weight matrices for lesion region and background region, respectively; and

$$\boldsymbol{M}_L = \left[\int_L \Delta\mu_a(r')\,\mathrm{d}^3 r', \ldots, \int_{N_L} \Delta\mu_a(r')\,\mathrm{d}^3 r'\right]$$

and

$$\boldsymbol{M}_B = \left[\int_B \Delta\mu_a(r')\,\mathrm{d}^3 r', \ldots, \int_{N_B} \Delta\mu_a(r')\,\mathrm{d}^3 r'\right]$$

are the total absorption distribution of the lesion and the background regions, respectively. Here, the total absorption distribution was reconstructed rather than $\Delta\mu_a(r')$. At the end of the iterative optimization, the total absorption distribution is divided by the different voxel sizes of the lesion and background to obtain $\Delta\mu_a(r')$. This method significantly reduced the background artifacts because the voxel size in the background area was much larger than that in the lesion area.

For an inhomogeneous concentric target, the inner core size of the reconstructed image was measured as 2 times of the mean value of r_x and r_y (as shown in Fig. 3), where r_x was measured between the (maximum + minimum)/2 and the minimum of the absorption curve along the x axis, and r_y was measured similarly along the y axis.

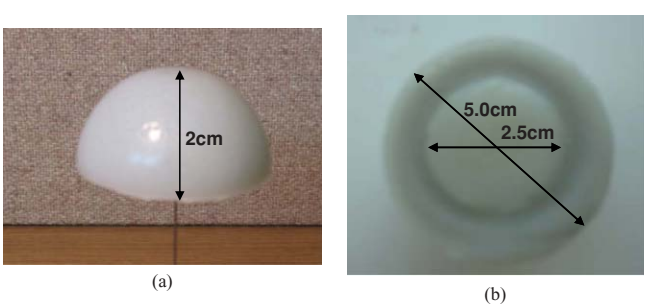

Fig. 4 Example of a concentric semiellipsoidal target phantom: (a) front view and (b) bottom view of the phantom.

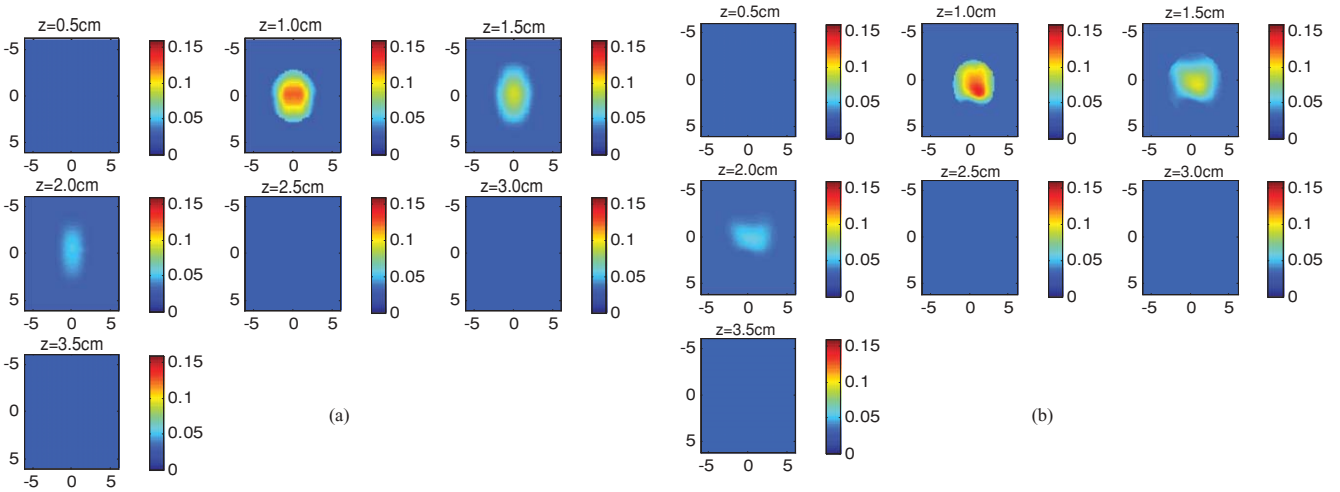

Fig. 5 Reconstruction results of a concentric semiellipsoidal target with a diameter of 5 cm and a height of 2 cm: (a) simulation and (b) phantom experiment.

2.3 *Experiment*

Phantoms of different sizes with different optical properties were made using polyvinyl chloride-plastisol (PVCP) solution, which was a white opaque solution and became translucent when it was heated to a high temperature.[32] When the solution was gradually heated, the India ink and titanium dioxide (TiO_2) powder were added to control the optical absorption and scattering coefficients of the phantom. The heated solution was poured into

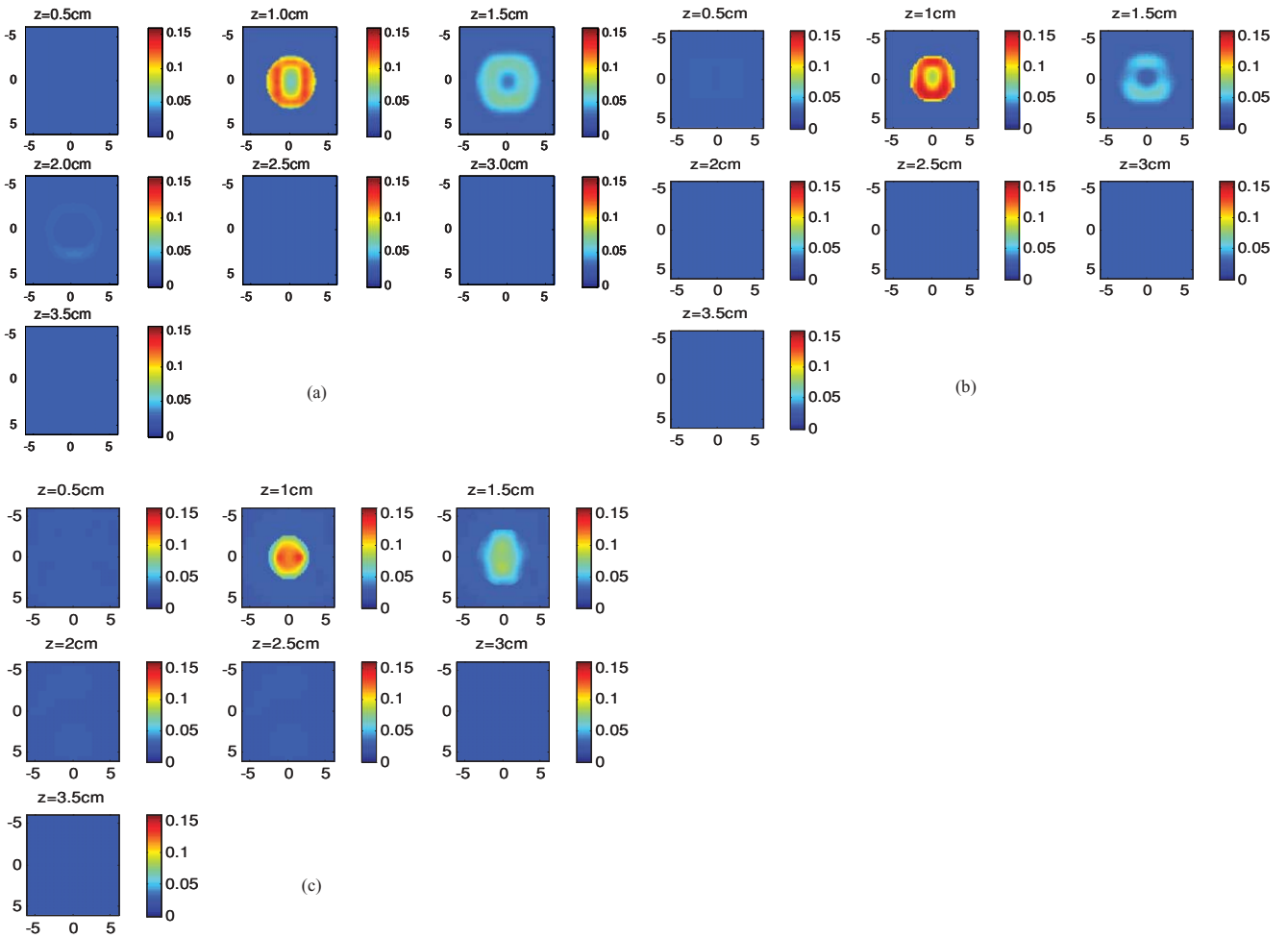

Fig. 6 Simulation results of a concentric semiellipsoidal target of outer shell diameter 5 cm, inner core diameter 2.5 cm, and height 2 cm of different layer thicknesses (a) 0.5, (b) 0.8, and (c) 1.0 cm.

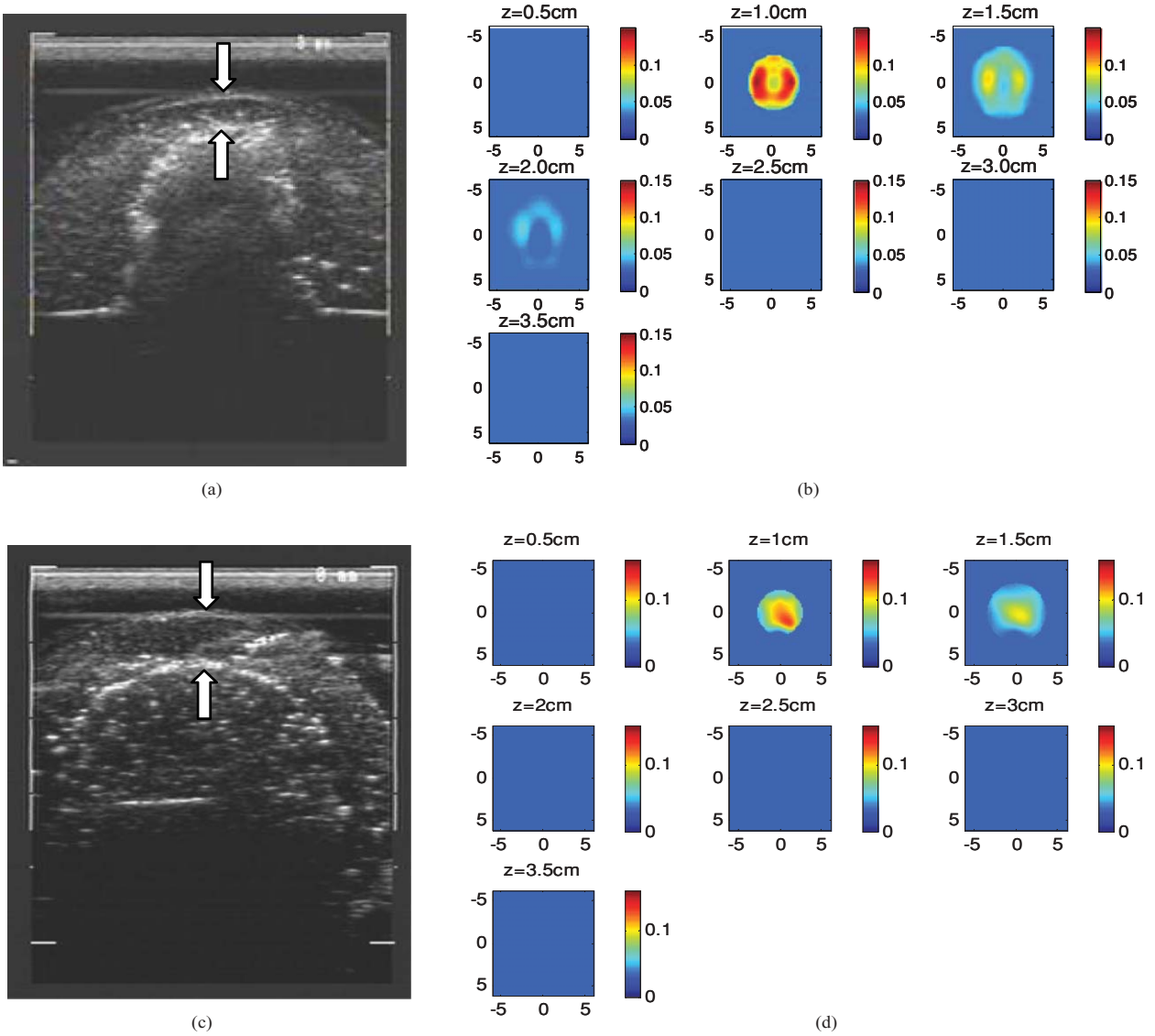

Fig. 7 Phantom experimental results of a concentric semiellipsoidal target of outer shell diameter 5 cm, inner core diameter 2.5 cm, and height 2 cm of different layer thickness (a) and (b) 0.5 cm and (c) and (d) 1.0 cm. (a) and (c) are US images and (b) and (d) are the corresponding absorption maps.

molds of a semiellipsoidal shape and solidified after cooling for several hours. For the special case of a larger target with different inner core optical properties, we made smaller targets first, and then proceeded the second time to make the larger target by embedding the smaller ones inside. Thus, the target outer shell and inner core had different optical properties. An example of a concentric semiellipsoidal target phantom is given in Fig. 4. The refractive index of the PVCP was reported in the literature[33,34] and the range at closer to room temperatures was from 1.44 to 1.54. MC simulations were performed to evaluate the effect of refractive index difference between the PVCP target and Intralipid solution on reconstructed target absorption. The maximum difference in reconstructed absorption was about 0.02 cm^{-1} when the solid phantom of $\mu_a = 0.25$ cm^{-1} and liquid background and inner core of $\mu_a = 0.03$ cm^{-1} were used. No change in target absorption distribution was observed.

Our frequency domain system consisted of 14 parallel detectors and four laser diodes of 740, 780, 808 and 830 nm. Each laser diode was sequentially switched to nine positions on the probe [see Fig. 1(a)]. The center slot on the probe was used for the US transducer and the sources and detectors were distributed on both sides. Intralipid solution was used to emulate the background tissue. Measurements were made with the target inside the Intralipid (target data) and intralipid alone as a reference. The target was supported by a 6- to 7-cm-long optical fiber mounted on a piece of white clay located at the bottom of a 2-l-capacity tank filled with Intralipid. The perturbation between the target data and the reference was used for imaging reconstruction. To compare reconstruction results with the closer-to-center source illumination when imaging a large semiellipsoidal inhomogeneous target, we also imaged the same target using the probe geometry shown in Fig. 1(b). In this geometry, two sources from the left side of the probe were moved to the top and bottom sides of the US transducer location. The objective of the second set of measurements was to estimate the effect of sources near the center on imaging reconstruction.

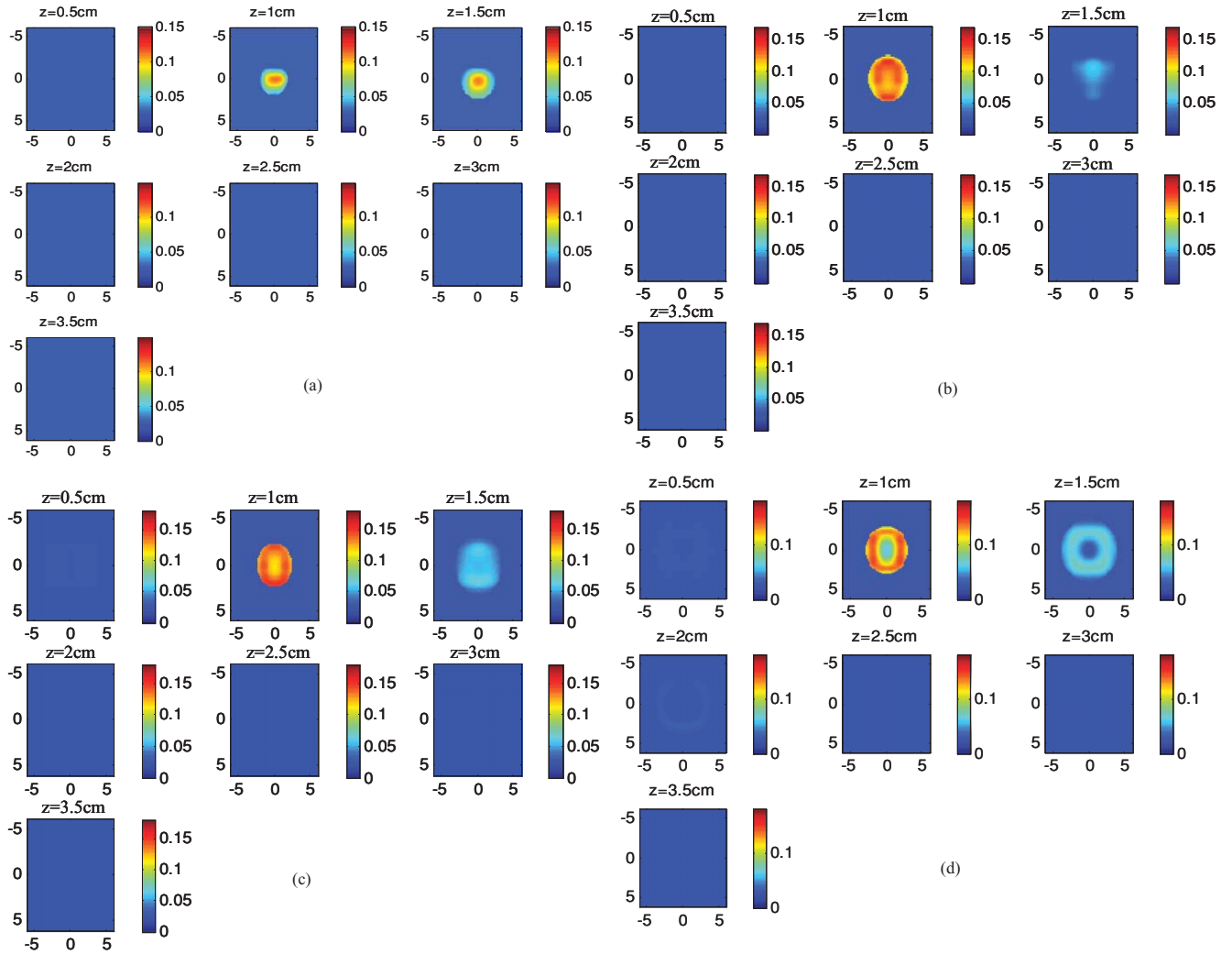

Fig. 8 Simulation results of concentric semiellipsoidal targets with fixed layer thickness $t = 0.5$ cm and different target sizes: (a) outer shell diameter of 2.5 cm and inner core diameter of 1.5 cm; (b) outer shell diameter of 3 cm and inner core diameter of 2 cm; (c) outer shell diameter of 3.5 cm and inner core diameter of 2.5 cm; and (d) outer shell diameter of 5 cm and inner core diameter of 4.0 cm.

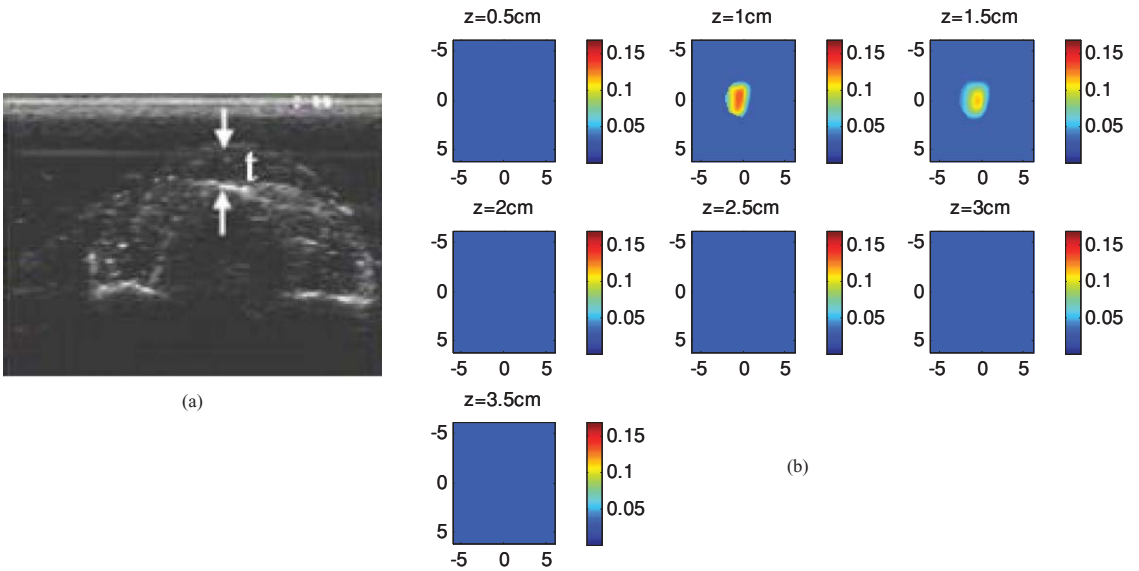

Fig. 9 Phantom result of a small concentric semiellipsoidal target with an outer shell diameter of 2.5 cm, an inner core diameter of 1.5 cm, a height of 1.5 cm, and a layer thickness of 0.5 cm. (a) US image and (b) reconstructed absorption map.

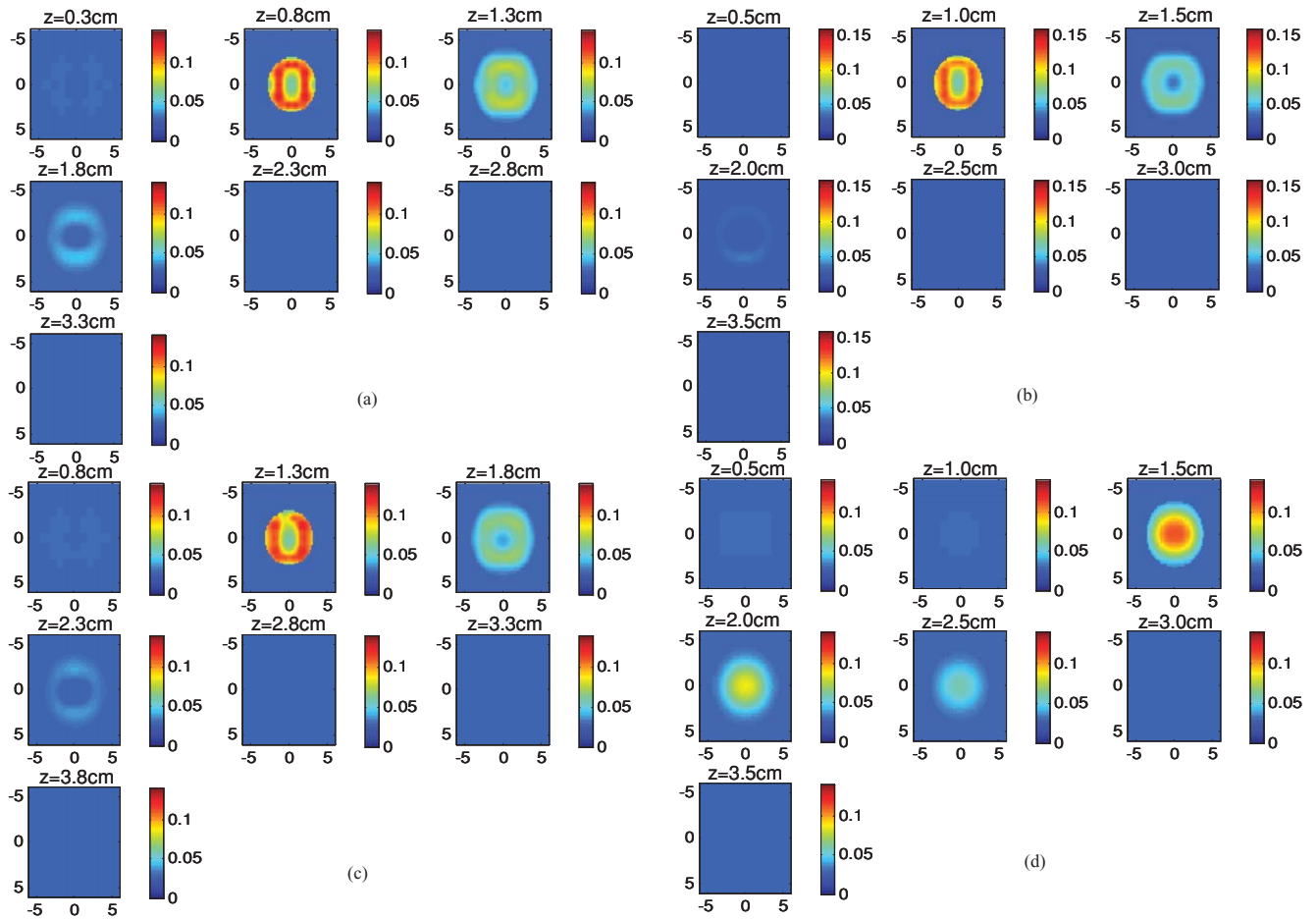

Fig. 10 Simulation results of a concentric semiellipsoidal target of outer shell diameter 5 cm, inner core diameter 2.5 cm, height 2 cm, and layer thickness 0.5 cm located at different depths. The distances between the bottom of the target and the probe surface were (a) 2.3, (b) 2.5, (c) 2.8, and (d) 3.0 cm. The probe of Fig. 1(b) was used for image reconstruction.

Clinical experiments were performed with the system of same design as that used for phantom experiments. The study protocol was approved by the local Institution Review Board (IRB) committee. All patients who participated in our study signed the informed consent. The patients' data were taken at the lesion area and the contralateral breast of the same quadrant as the lesion. The contralateral data set was used to estimate background optical properties for weight matrix computation. The perturbation was computed between lesion data and contralateral data and used for imaging reconstruction.

3 Results

In this section, five sets of simulations and experiments are reported in Sec. 3.1 to 3.5 and the clinical example is given in Sec. 3.6. The first set of simulations and experiments was performed using a homogeneous target. The result can serve as a baseline to compare with that obtained from an inhomogeneous target of a semiellipsoidal shape of different outer shell and inner core optical properties. The second set of simulations and experiments was performed to investigate two important target parameters that affect the resolving capability of the optical tomography. The third set of simulations and experiments was designed to emulate the condition that a tumor with fixed outer-shell to inner-core contrast was located at different depths. The range of the target depths investigated was from 1.0 to 3.0 cm, which was often encountered in the clinical studies when patients were scanned in a supine position. The fourth set of simulations and experiments was targeted to evaluate how the absorption of the inner core could affect the reconstructed contrast ratio of outer shell to inner core as well as the measured inner core size. In clinical studies, the center tumor core could have different absorption, lower than the periphery, due to rapid growth of the malignant cancer. The fifth set of the simulations and experiments was designed to investigate the effect of inner core diameter change on reconstructed contrast ratio of outer shell to inner core as well as measured inner core size. In clinical studies, we often encounter a necrotic core of dead tumor tissue of different size while the malignant tumor cells grow outward. At the end, we show a clinical example of a larger cancer imaged by our system.

3.1 *Homogeneous Targets*

In this section, we show MC simulation and phantom results of a homogeneous target, which can be used as a baseline to compare with that of inhomogeneous targets.

In the MC simulation, a 5-cm-diam, 2-cm-high semiellipsoidal target had optical properties of absorption coefficient

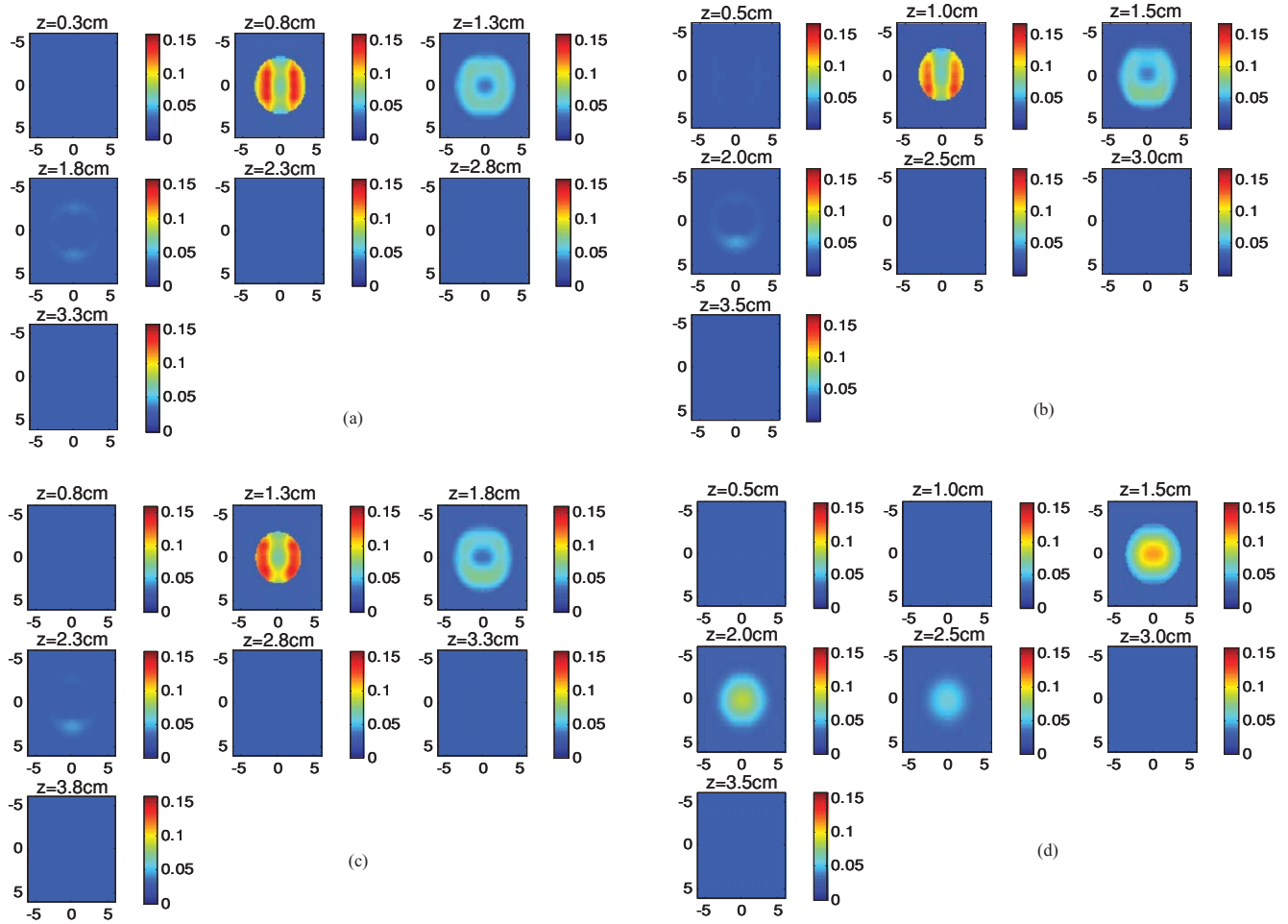

Fig. 11 Simulation results of a concentric semiellipsoidal target of outer shell diameter 5 cm, inner core diameter 2.5 cm, height 2 cm, and layer thickness 0.5 cm located at different depths. The distances between the bottom of the target and the probe surface were (a) 2.3, (b) 2.5, (c) 2.8, and (d) 3.0 cm. The probe of Fig. 1(a) was used for image reconstruction.

$\mu_a = 0.25$ cm^{-1} and reduced scattering coefficient $\mu_s' = 6.0$ cm^{-1}. The background properties were set to $\mu_a = 0.03$ cm^{-1} and $\mu_s' = 6.0$ cm^{-1}. The target bottom was located at a 2.5-cm depth from the surface. Figure 5(a) shows the reconstructed target absorption map. The probe shown in Fig. 1(b) was used for image reconstruction. Tomography images are shown in seven slices at different depths from 0.5 to 3.5 cm with a 0.5-cm increment in depth. The ROI is shown from the second slice and distributed in three layers at depths of 1.0, 1.5, and 2.0 cm. The distribution at each layer is quite uniform. The reconstructed maximum $\mu_a$was 0.13 cm^{-1}. A similar result was obtained from a phantom experiment, as shown in Fig. 5(b). The target had the same size and the same optical properties as the simulation and the reconstructed maximum absorption coefficient is 0.14 cm^{-1}. The absorption map at each layer is quite uniform.

3.2 *Effects of Target Parameters on Imaging Concentric Inhomogeneous Targets*

In this section, we evaluate two target parameters that are critical for imaging periphery enhancement absorption distribution. The thickness between the outer shell and the inner core t, shown in Fig. 2(a), is an important parameter for resolving the target inhomogeneity. In this set of simulation, a semiellipsoidal target was presented with outer diameter of 5.0 cm, an inner core diameter of 2.5 cm, a height h of 2.0 cm, and a t of 0.5, 0.8, and 1.0 cm, respectively. The target outer shell and inner core had same reduced scattering coefficient of $\mu_s' = 6.0$ cm^{-1} and different absorption coefficients of $\mu_a = 0.25$ cm^{-1} and 0.03 cm^{-1}. The target bottom was located at a 2.5-cm depth from the surface. The background optical properties were $\mu_a = 0.03$ cm^{-1} and $\mu_s' = 6.0$ cm^{-1}. Figure 6 shows the reconstructed target absorption maps of different layer thicknesses of 0.5, 0.8, and 1.0 cm, respectively. The probe shown in Fig. 1(b) was used for image reconstruction. The reconstructed maximum μ_as were 0.13, 0.14, and 0.13 cm^{-1}, respectively. Using the method introduced in Sec. 2.2, the measured inner diameters of the target region were 1.9, 1.4, and 0.3 cm. The corresponding phantom experiments were performed for the same size targets with layer thicknesses of 0.5 and 1.0 cm, respectively. Figure 7 shows the reconstruction results, which had the maxima $\mu_a = 0.15$ cm^{-1} and 0.13 cm^{-1}, respectively. When the thickness t is less than 1.0 cm, the inner core is visible. However, when t is larger than 1 cm, the inner core cannot be resolved, even the core diameter is relatively large. This is caused by the increased scattering events

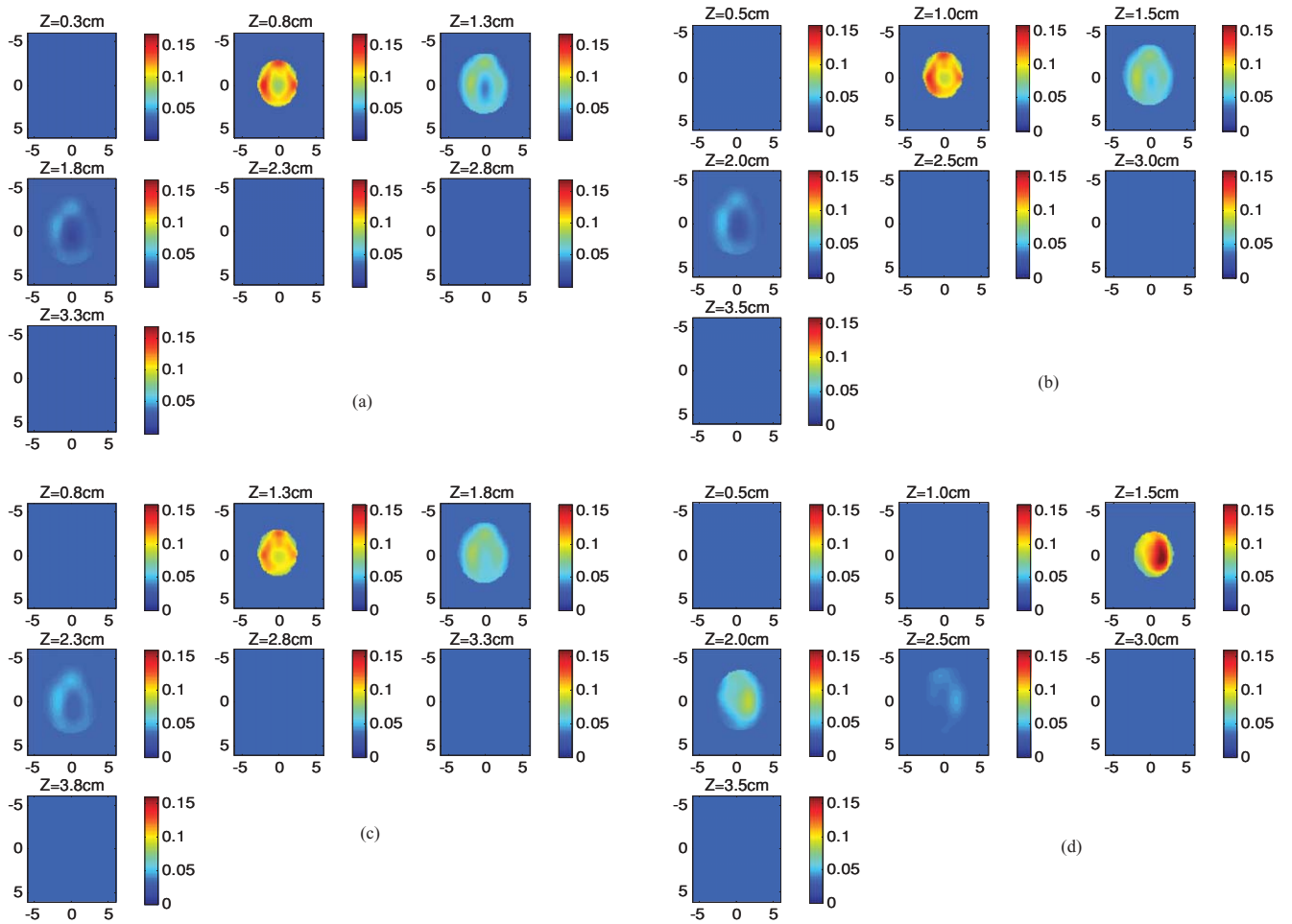

Fig. 12 Phantom results of a concentric semiellipsoidal target with an outer shell diameter of 5 cm, an inner core diameter of 2.5 cm, a height of 2 cm, and a layer thickness of 0.5 cm located at different depths. The distances between the bottom of the target and the probe surface were (a) 2.3, (b) 2.5, (c) 2.8, and (d) 3.0 cm. The probe of Fig. 1(b) was used for image reconstruction.

when photons pass an outer shell more than 1 cm thick and the information loss between the two groups of photons passing the outer shell only and passing the outer shell and the inner core.

Another important parameter is the target size. A series of MC simulations was performed by fixing t to 0.5 cm and varying the target size from 2.5 to 5 cm. The reconstruction results were shown in Fig. 8. Figures 8(a) to 8(d) are the absorption maps of the 2.5-, 3.0-, 3.5-, and 5.0-cm-diam targets with 1.5-, 2.0-, 2.5-, and 4.0-cm inner core sizes, respectively. The probe shown in Fig. 1(b) was used for imaging reconstruction. The target bottom was located at 2.5 cm. The maximum absorption coefficients were 0.14, 0.14, 0.15, and 0.14 cm^{-1}, respectively. The reconstructed inner diameters were 0.0, 1.2, 1.8, and 2.6 cm, respectively. As one can see, the target size must be larger than 3 cm for the resolving target outer shell and inner core. The simulation results were validated by experiments. An example of a 2.5-cm-diam target with a 1.5-cm inner core size was shown in Fig. 9. In this example, the target inner core cannot be resolved.

Based on the simulations and experiments, we used $t = 0.5$ cm layer thickness and a 5-cm target diameter for all simulations and experiments reported in the following sections to investigate the effect of other parameters on imaging target inhomogeneity.

3.3 *Inhomogeneous Target Located at Different Depths*

This set of experiments was designed to investigate the target depth on the reconstructed contrast of a target having a fixed outer shell to inner core absorption ratio and the measured inner core diameter. The target depths evaluated were in the range of 1 to 3 cm, which we often encounter in the clinical studies.

A semiellipsoidal target presented in this set of simulation had an outer diameter of 5 cm, an inner core diameter of 2.5 cm, a height of 2 cm, and a t of 0.5 cm. The target outer shell and inner core had same reduced scattering coefficient of $\mu_s' = 6.0\ cm^{-1}$ and different absorption coefficients of $\mu_a = 0.25\ cm^{-1}$ and $0.06\ cm^{-1}$, respectively. The background optical properties were set to $\mu_a = 0.03\ cm^{-1}$ and $\mu_s' = 6.0\ cm^{-1}$. Figure 10 shows the reconstructed absorption maps of the target with the bottom of the target located at 2.3, 2.5, 2.8, and 3.0 cm from the probe surface, respectively. The probe with closer-to-center sources shown in Fig. 1(b) was used to obtain the measurements. The reconstructed maximum μ_as were 0.12, 0.13, 0.12, and 0.11 cm^{-1}, respectively, which were quite close at all depths studied. The measured inner diameters were 1.9, 1.9, 1.5, and 0.0 cm, respectively. The periphery of the target

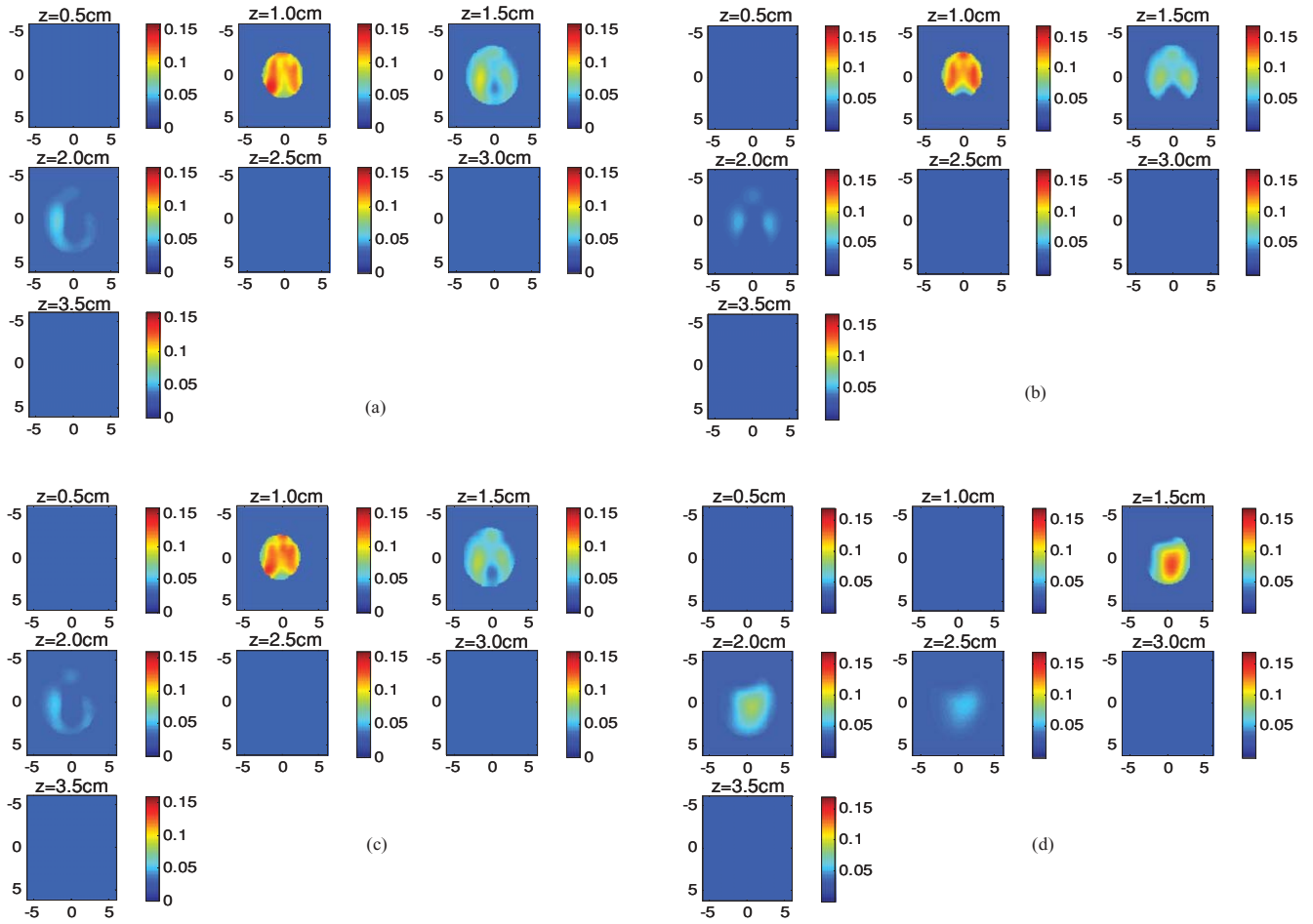

Fig. 13 Phantom results of a semiellipsoidal target with an outer shell diameter of 5 cm, an inner diameter of 2.5 cm, a height of 2 cm, and a layer thickness of 0.5 cm located at different depths. The distances between the bottom of the target and the probe surface were (a) 2.3, (b) 2.5, (c) 2.8, and (d) 3.0 cm. The probe of Fig. 1(a) was used for image reconstruction.

showed higher absorption than the inner core for the first three sets of experiments and the periphery enhancement disappeared when the target was located deeper [Fig. 10(d)]. The ring shape was ideally seen in the reconstructed absorption map at different target layers in Figs. 10(a) to 10(c). In our clinical studies, the center slot dimension was adapted to the commercial US transducer used and the space for center sources was limited. To evaluate how much closer-to-center sources can affect the reconstructed target inhomogeneity, we used the probe without center sources to perform the simulation again. Figure 11 shows the reconstruction results of the same target located at the same corresponding depths as in Fig. 10. The reconstructed maximum μ_as were 0.14, 0.14, 0.14, and 0.11 cm^{-1}, respectively. We can clearly see that the absorption at the first target layer was higher at the two sides where the sources were distributed [Figs. 11(a) to 11(c)]. However, the higher absorption at both sides of the target was clearly visible. We can see that the maximum reconstructed values were quite close at the depths studied, however, the measured inner diameter became smaller and smaller when the target was deeper. When the target bottom reached 3.0 cm, the outer and inner layers merged.

A phantom experiment was performed under conditions similar to those in the simulation. The Intralipid solution of calibrated $\mu_a = 0.03$ cm^{-1} and $\mu_s' = 7.2$ cm^{-1} at a 780-nm wavelength was used as the background. The target shown in Fig. 4 had an outer shell diameter of 5.0 cm, an inner core diameter of 2.5 cm, a height h of 2.0 cm, and a t of 0.5 cm. The shell had $\mu_a = 0.25$ cm^{-1} and $\mu_s' = 7.1$ cm^{-1}, and the core had $\mu_a = 0.06$ cm^{-1} and $\mu_s' = 5.2$ cm^{-1}. Figure 12 shows the reconstruction results of the target located at different depths using the probe shown in Fig. 1(b). Figures 12(a) to 12(d) show the reconstructed absorption maps when the target was located at depths corresponding to those in the Fig. 10. The reconstructed maximum μ_as were 0.15, 0.14, 0.13, and 0.15 cm^{-1}, respectively. The reconstructed inner core diameters were 2.0, 2.0, 1.4, and 0.0 cm, respectively. When the target bottom was located at 3.0 cm, the outer and inner regions were merged and target appeared to be homogeneous.

To verify the simulation results without center sources, we used the probe shown in Fig. 1(a) to obtain data of the same target at the same depths as used for Fig. 12. The result is shown in Fig. 13. The reconstructed maximum μ_as were 0.14, 0.14, 0.13, and 0.14 cm^{-1}, respectively, which are very close to those obtained from Fig. 12. The ring pattern is clearly visible, however, the shape is not as good as the one obtained with the center sources shown in Fig. 12.

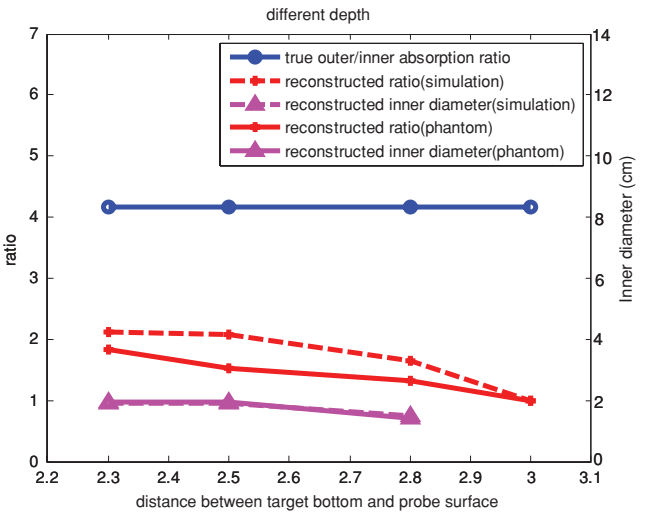

Fig. 14 Plot of contrast ratio (left *y* axis) and reconstructed inner diameter (right *y* axis) versus target depths.

Figure 14 provides a more quantitative comparison of both simulation and phantom experiments. As given before, the true μ_as of the outer shell and inner core for both simulation and experiment were $\mu_a = 0.25\ \text{cm}^{-1}$ and $0.06\ \text{cm}^{-1}$, so the true ratio was 4.17. The reconstructed ratio was defined as the maximum value over the minimum value inside the target region. The reconstructed ratios for simulation shown in Figs. 10(a) to 10(d) were 2.12, 2.08, 1.66, and 1.0, respectively. The corresponding ratios for the experiment shown in Fig. 12 were 1.83, 1.53, 1.32, and 1.0, respectively. The true inner diameters for both simulation and phantom experiments were 2.5 cm. The measured inner diameters were 1.9, 1.9, and 1.5 cm, respectively, in Figs. 10(a) to 10(c); and the corresponding measured values were 2.0, 2.0, and 1.4 cm, respectively, in Figs. 12(a) to 12(c). As expected, when the target depth increased, the reconstructed ratio as well as the measured inner diameter reduced because of the received photons that passed through the outer shell only and the outer shell and inner core went through more scattering events. As a result, the location information that these two groups of photons carried was lost in the scattering process.

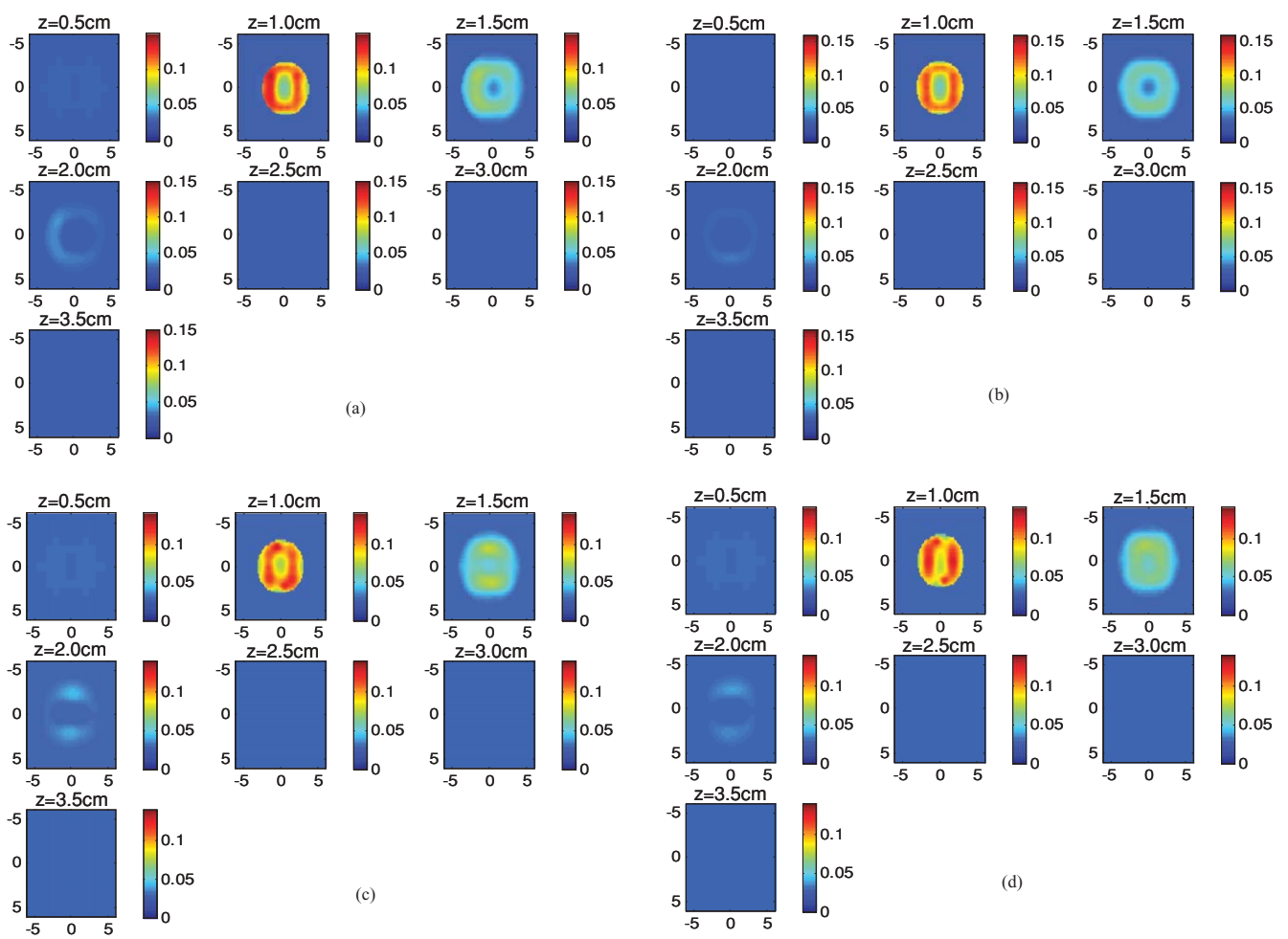

Fig. 15 Simulation results of a concentric semiellipsoidal target of outer shell diameter 5 cm, inner core diameter 2.5 cm, height 2 cm, and layer thickness 0.5 cm with different inner core absorption coefficients. The probe shown in Fig. 1(b) was used for image reconstruction. The inner core absorption coefficients were (a) 0.03, (b) 0.06, (c) 0.08, and (d) 0.15 cm^{-1}, respectively.

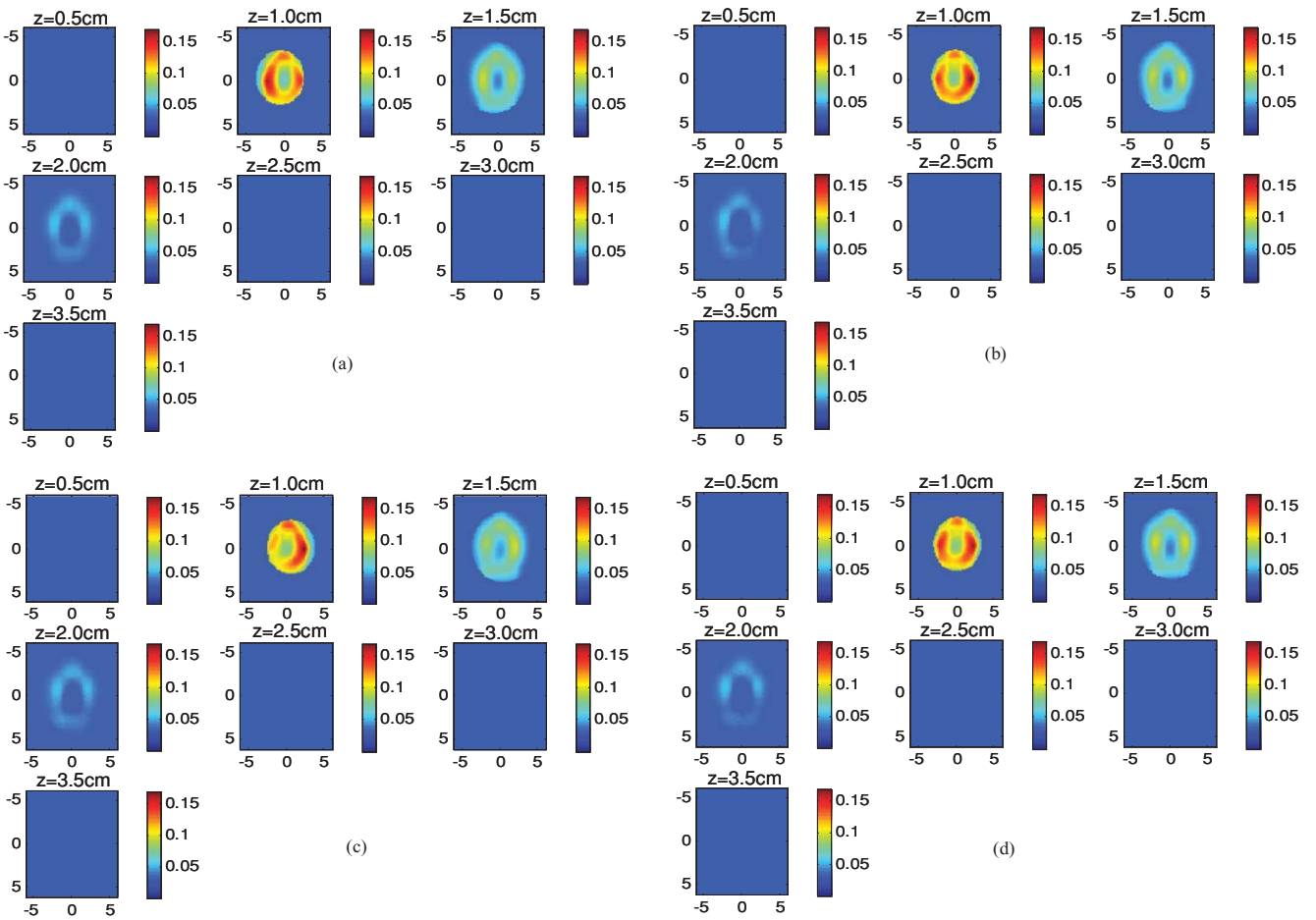

Fig. 16 Phantom results of a concentric semiellipsoidal target of outer shell diameter 5 cm, inner diameter 2.5 cm, height 2 cm, and layer thickness 0.5 cm with different inner core absorptions imaged. The probe shown in Fig. 1(b) was used for image reconstruction. The inner core absorption coefficients were (a) 0.03, (b) 0.06, (c) 0.08, and (d) 0.15 cm^{-1}, respectively.

3.4 *Inhomogeneous Target with Different Innercore Absorption*

This set of simulation and phantom experiment demonstrates how the absorption of the inner core affects the reconstructed contrast ratio of the outer shell to the inner core as well as the measured inner core size. Both MC simulation and phantom experiments were performed under similar conditions. In clinical studies, the center tumor core could have a different absorption, lower than the periphery, due to rapid growth of the malignant cancer.

In this set of simulation, the semiellipsoidal target had an outer diameter of 5 cm, an inner core diameter of 2.5 cm, an h of 2 cm, and a t of 0.5 cm. The absorption coefficient of the outer layer was fixed to $\mu_a = 0.25$ cm^{-1} and the inner core μ_a were changed to 0.03, 0.06, 0.08, and 0.15 cm^{-1}, respectively. The reduced scattering coefficient of both shell and core is the same as $\mu_s' = 6.0$ cm^{-1}. The target bottom was located at 2.5 cm from the probe surface. The background properties were $\mu_a = 0.03$ cm^{-1} and $\mu_s' = 6.0$ cm^{-1}. Figure 15 shows the reconstruction results of the target with fixed outer layer absorption and different inner core absorption using the probe shown in Fig. 1(b). As shown in Fig. 15, the reconstructed maximum μ_as were 0.14, 0.13, 0.13, and 0.13 cm^{-1}, respectively. The reconstructed inner diameters of the center region were 2.0, 1.9, 1.5, and 1.5 cm, as shown in Figs. 15(a) to 15(d). As expected, the inner core absorption does not affect the reconstructed maximum value because the outer shell absorption was fixed. However, as the inner core absorption increases, the contrast ratio of the shell and the core decreases and the measured inner diameter reduces. If we used the probe without center sources, as shown in Fig. 1(a), the maximum μ_as were 0.14, 0.14, 0.13, and 0.13 cm^{-1}, respectively. Similar to the results shown in Sec. 3.3, the probe shown in Fig. 1(b) with the center sources reconstructs the target shape better than that of probe shown in Fig. 1(a); while the reconstructed maximum μ_as were very similar using both probes.

The phantom target was made of fixed outer shell absorption $\mu_a = 0.25$ cm^{-1} and reduced scattering coefficient $\mu_s' = 7.1$ cm^{-1}, but different inner core values $\mu_a = 0.03$, 0.06, 0.08, and 0.15 cm^{-1}, respectively, and reduced scattering coefficients of $\mu_s' = 7.2$, 5.2, 7.9, and 9.0 cm^{-1}, respectively. Similar to the simulation, the outer target diameter was 5 cm, the inner core was 2.5 cm, $h = 2$ cm, and $t = 0.5$ cm. Figures 16 shows the reconstruction results of a target of different inner core absorption coefficients. The Intralipid solution used as the background had $\mu_a = 0.03$ cm^{-1} and $\mu_s' = 7.2$ cm^{-1} at a 780-nm wavelength. The probe shown in Fig. 1(b) with

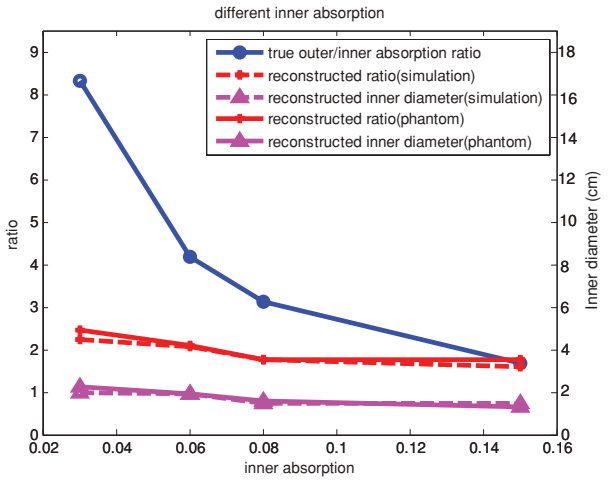

Fig. 17 Plot of contrast ratio (left *y* axis) and reconstructed inner diameter (right *y* axis) versus different inner core absorption.

center sources was used. In Figs. 16(a) to 16(d), the reconstructed maximum μ_as were 0.16, 0.17, 0.17, and 0.17 cm^{-1}, respectively. Similar to the simulation, the maximum values do not change much with the different inner core absorption coefficients. However, the measured inner core diameters were 2.2, 1.9, 1.6, and 1.3 cm, accordingly. The measured inner core diameter reduces as the target contrast of the outer shell and the inner core decreases. A reconstructed absorption map using the probe given in Fig. 1(a) has maximum μ_as 0.15, 0.16, 0.16, and 0.17 cm^{-1}, respectively, which were very close to the corresponding values given in Fig. 16. However, the ring shape of the target was not as good as shown in Fig. 16.

Figure 17 compares the simulation and phantom experiments for targets with different outer shell and inner core contrasts. The dashed lines represent simulation results and the solid lines are those of the phantom experiments. Three groups of data are true contrast ratio, reconstructed ratio of outer shell over inner core absorption coefficients, and measured inner core diameters. As one can see, the experimental results agree well with simulation data.

For both simulation and phantom experiments, the true ratios of outer shell to inner core absorption were 8.33, 4.17, 3.13, and 1.67, respectively. The reconstructed ratio was the measured maximum absorption over the minimum inside the target region. The reconstructed ratios of the simulation were 2.25, 2.08, 1.75, and 1.59 for inner core $\mu_a = 0.03$, 0.06, 0.08, and 0.15 cm^{-1}, respectively. These ratios were 2.46, 2.10, 1.78,

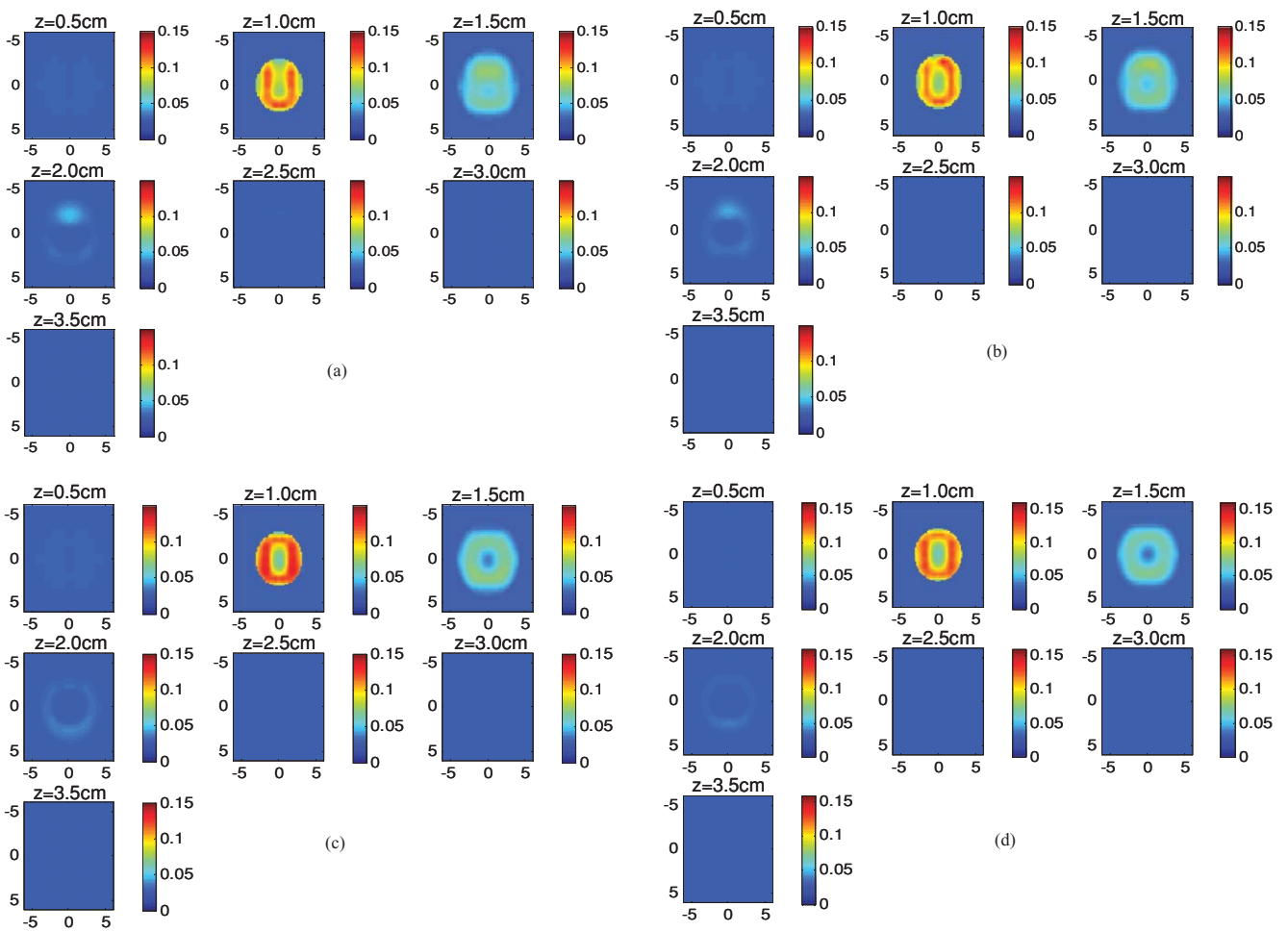

Fig. 18 Simulation results of a concentric semiellipsoidal target of outer shell diameter 5 cm, inner core diameter 2.5 cm, height 2 cm, and layer thickness 0.5 cm of different inner core diameters. The probe shown in Fig. 1(b) was used for image reconstruction. Inner core diameters were (a) 1.0, (b) 1.5, (c) 2.0, and (d) 2.5 cm.

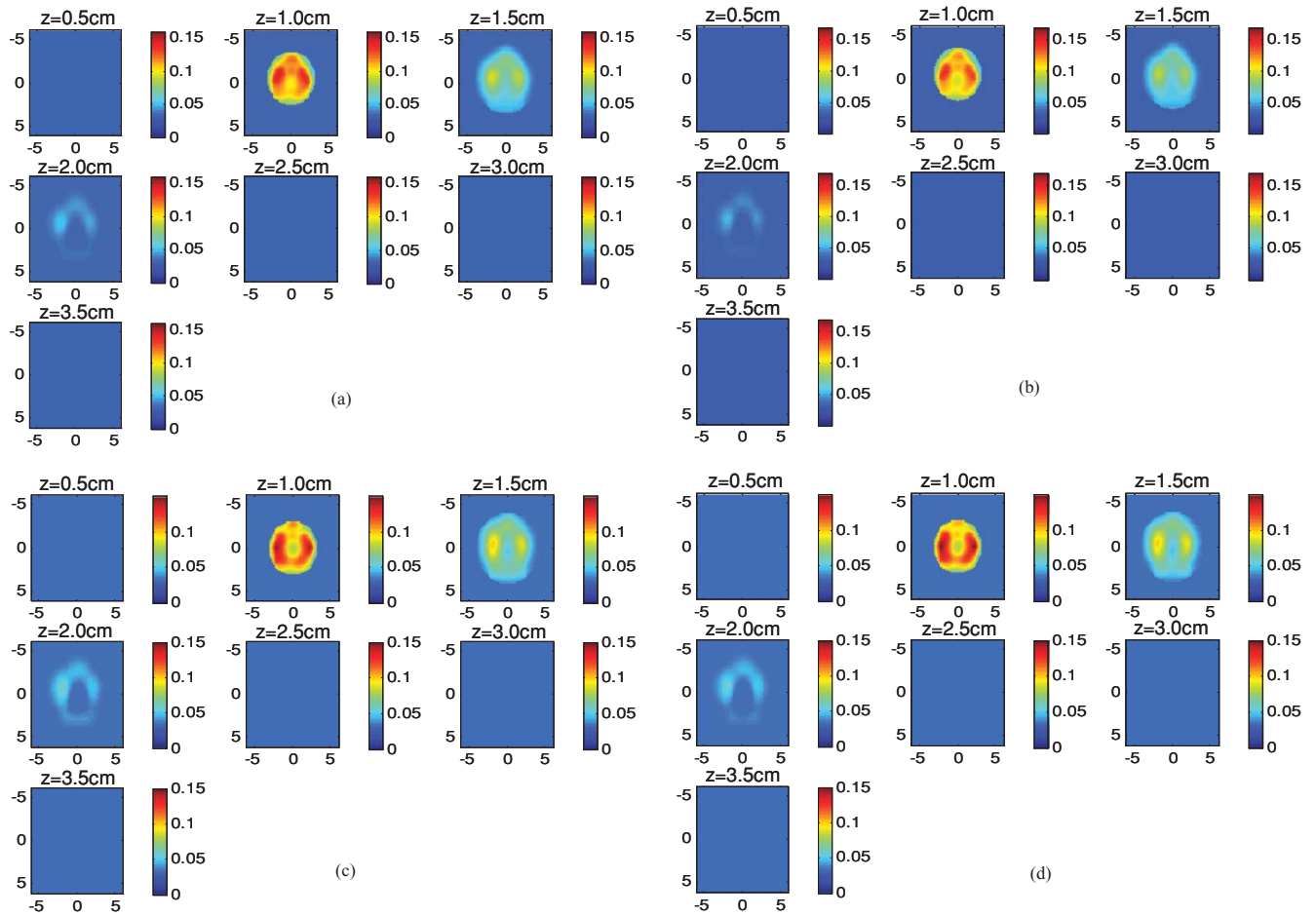

Fig. 19 Phantom results of a concentric semiellipsoidal target of outer shell diameter of 5 cm, inner core diameter of 2.5 cm, height of 2 cm, and layer thickness 0.5 cm of different inner core diameters. The probe shown in Fig. 1(b) was used for image reconstruction. Inner diameters were (a) 1.0, (b) 1.5, (c) 2.0, and (d) 2.5 cm.

and 1.77, respectively, as measured in the experiments. The measured inner diameters were 2.0, 1.9, 1.5, and 1.5 cm in the simulation, respectively, while the measured diameters were 2.2, 1.9, 1.6, and 1.3 cm, respectively, in the experiments. Note that the true ratio of outer shell to inner core absorption reduces rapidly with the increase of inner core absorption; however, the reconstructed ratio in both simulation and experiments reduces gradually. Because of the intense scattering of photons in the turbid medium, the reconstructed ratios can reach only about a factor of 2. The measured inner diameter also reduces with the increase of inner core absorption.

3.5 *Inhomogeneous Target with Different Inner Diameter*

This set of experiments was designed to investigate the effect of inner core diameter change on reconstructed contrast ratio of outer shell and inner core optical absorptions as well as measured inner core size.

The target had fixed outer shell and inner core optical properties of $\mu_a = 0.25\,\mathrm{cm}^{-1}$ and $\mu_s' = 6.0\,\mathrm{cm}^{-1}$ and $\mu_a = 0.03\,\mathrm{cm}^{-1}$ and $\mu_s' = 6.0\,\mathrm{cm}^{-1}$, respectively. The outer diameter and layer thickness t were fixed to 5 and 0.5 cm, respectively, and the core diameters were changed from 1.0 to 1.5, 2, and 2.5 cm, respectively. The background properties were $\mu_a = 0.03\,\mathrm{cm}^{-1}$ and $\mu_s' = 6.0\,\mathrm{cm}^{-1}$. The simulations were processed with center sources, as shown in Fig. 1(b). Figure 18 shows the reconstructed image. Figure 18(a) is the image of target with a 1.0-cm inner core diameter. The maximum value of μ_a was $0.12\,\mathrm{cm}^{-1}$ and the measured inner core diameter was 1.5 cm. Figures 18(b) to 18(d) are the reconstructed images with 1.5-, 2.0-, and 2.5-cm inner core diameters, respectively. The corresponding measured maximum absorption were 0.13, 0.13, and $0.13\,\mathrm{cm}^{-1}$; while the measured inner core diameters were 1.52, 1.9, and 1.9 cm, respectively. As expected, the maximum reconstructed values are similar because of the fixed absorption of the outer shell, and the reconstructed inner core diameter increases with the increase of the inner core diameter size.

To validate the simulation results, phantom experiments with the similar condition were performed. Because of the difficulty of making different phantoms with exactly the same inner core size as the simulation, we used the same phantom by gradually enlarging the inner core size to perform the experiments. To do so, the optical properties of the outer shell and inner core did not change and the only variable was the inner core size. The optical properties of the outer shell were $\mu_a = 0.25\,\mathrm{cm}^{-1}$ and $\mu_s' = 7.1\,\mathrm{cm}^{-1}$, the diameter was 5 cm, and the t was 0.5 cm. The inner core was filled with Intralipid solution of calibrated

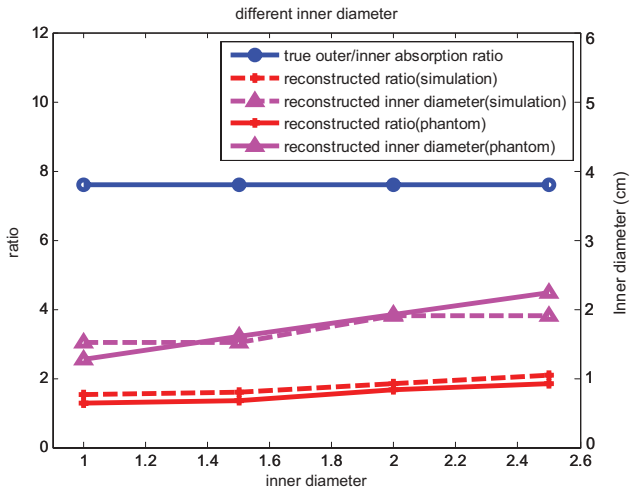

Fig. 20 Plot of contrast ratio (left y axis) and reconstructed inner diameter (right y axis) versus the inner core diameter.

$\mu_a = 0.03\ \text{cm}^{-1}$ and $\mu_s' = 7.2\ \text{cm}^{-1}$. Experiments for four different inner core diameters of 1.0, 1.5, 2, and 2.5 cm were performed with results shown in Fig. 19(a) to 19(d), respectively. The probe of Fig. 1(b) was used for this set of experiments. The reconstructed maximum μ_as in Figs. 19(a) to 19(d) were 0.14, 0.15, 0.14, and 0.15 cm^{-1}, respectively; while the measured inner core diameters were 1.3, 1.6, 1.9, and 2.2 cm, respectively. The phantom experiments closely followed the simulation, and further demonstrated that maximum values do not change much for the fixed outer layer, however, the measured inner diameter increases with the increase of the true hollow inner core size.

Figure 20 shows the simulation and phantom experimental results for targets with different inner diameters. The dashed lines represent simulation results and the solid lines are those of the phantom experiments. The three groups of data are true absorption ratio, reconstructed ratio of outer shell over inner core absorptions, and measured inner core diameter for target of different inner core size. The true contrast ratio of outer shell over inner core absorption was 7.6. The reconstructed ratios from simulations were 1.52, 1.60, 1.84, and 2.08, respectively; these values were 1.28, 1.34, 1.68, and 1.84 for experiments. The measured diameters were 1.5, 1.5, 1.9, and 1.9 cm in simulation, and were 1.3, 1.6, 1.9, and 2.2 cm in experiments, respectively. Comparing the reconstructed ratios with the true ratio, we see that the reconstructed ratios can reach only a factor of 2 and increase with the increase of the inner core diameter. Correspondingly, the measured inner core diameter increases with the increase of the true diameter size.

3.6 *Clinical Example*

A clinical example of an advanced cancer of approximately 4 cm size is given in Fig. 21. The coregistered US showed a highly suspicious mass located in the left breast at the 3 o'clock position of an 86-year-old woman. The lesion top and bottom were approximately located at 0.5- and 2.5-cm depths from the skin surface. US-guided biopsy reveled that the mass was a high-grade (nuclear grade II, histology grade III) invasive ductal carcinoma. Further evaluation of hematoxylin and eosin (H&E) stained histology slides showed extensive tumor necrosis, which occupied about 40% of the core biopsy samples. Optical absorption maps obtained at 780 nm [Fig. 21(b)] and 830 nm [Fig. 21(c)] showed a higher periphery contrast than the inner core area. The computed total hemoglobin concentration showed similar periphery enhancement of maximum and average concentrations of 86 and 55 μmol/L, respectively. This type of periphery enhancement is often seen in advanced cancers.

4 Discussion and Summary

Angiogenesis patterns of advanced breast cancers are complex, and there is no unique feature that can uniquely characterize these tumors. From our on-going clinical studies, we have seen two typical types of absorption or vasculature distribution patterns of advanced cancers: periphery enhancements or posterior shadowing.[22] More interestingly, the periphery enhancements are often seen in high-grade tumors,[22] which have been reported in MRI literature as well.[26,27] Posterior shadowing is caused by significant light absorption of a highly vascularized tumor, which causes a dramatic reduction of the reflected light received from the deeper portion of the tumor. As a result, the reconstructed absorption maps of these large tumors have shown much higher light absorption at the top portion than that of the deeper portion.[30] This shadowing effect is similar to the posterior shadowing seen in pulse-echo US when imaging larger tumors. The presence of significant posterior shadowing of a lesion in US images suggests malignance.[35]

To characterize and quantify periphery enhancement features of optical tomography when imaging these larger cancers, we performed five sets of simulations and phantom experiments in the reported study. As shown in the studies, two target parameters affect the resolving capability of optical tomography: the layer thickness between the outer shell and the inner core and the target size. To resolve the inner core, the layer thickness must be less than 1 cm and the target size must be larger than 3 cm. Concentric inhomogeneous targets of thicker layers and smaller diameters may not show periphery enhancement features in images. This result may explain why we have observed the periphery enhancement in advanced cancers of high-grade tumors, which grow rapidly outward with extensive dead necrotic core. In addition, the periphery enhancement occurs at target depths less than 3 cm. Deep concentric inhomogeneous targets may not show this feature in images due to intense light scattering in tissue. Therefore, quantifying target parameters and target depth is critically important when using periphery enhancement features to assist US diagnosis of advance cancers. Certainly, these parameters may vary to some extend based on an individual patient's bulk absorption and scattering coefficients. The inner core optical absorption and size also affect imaging periphery enhancement features to some extent. The reported investigation on near-center source illumination also provides an important guideline for the probe design. As shown from the studies, two near-center sources at the top and bottom sides of the US probe are required to improve visualization for the target heterogeneity. This is feasible in the probe design using US guidance.

Because of the large target size studied, multiple fine-mesh target layers in depth were used in image reconstruction. As a result, more voxels with unknown optical properties were reconstructed and the lesion quantification was about 50 to

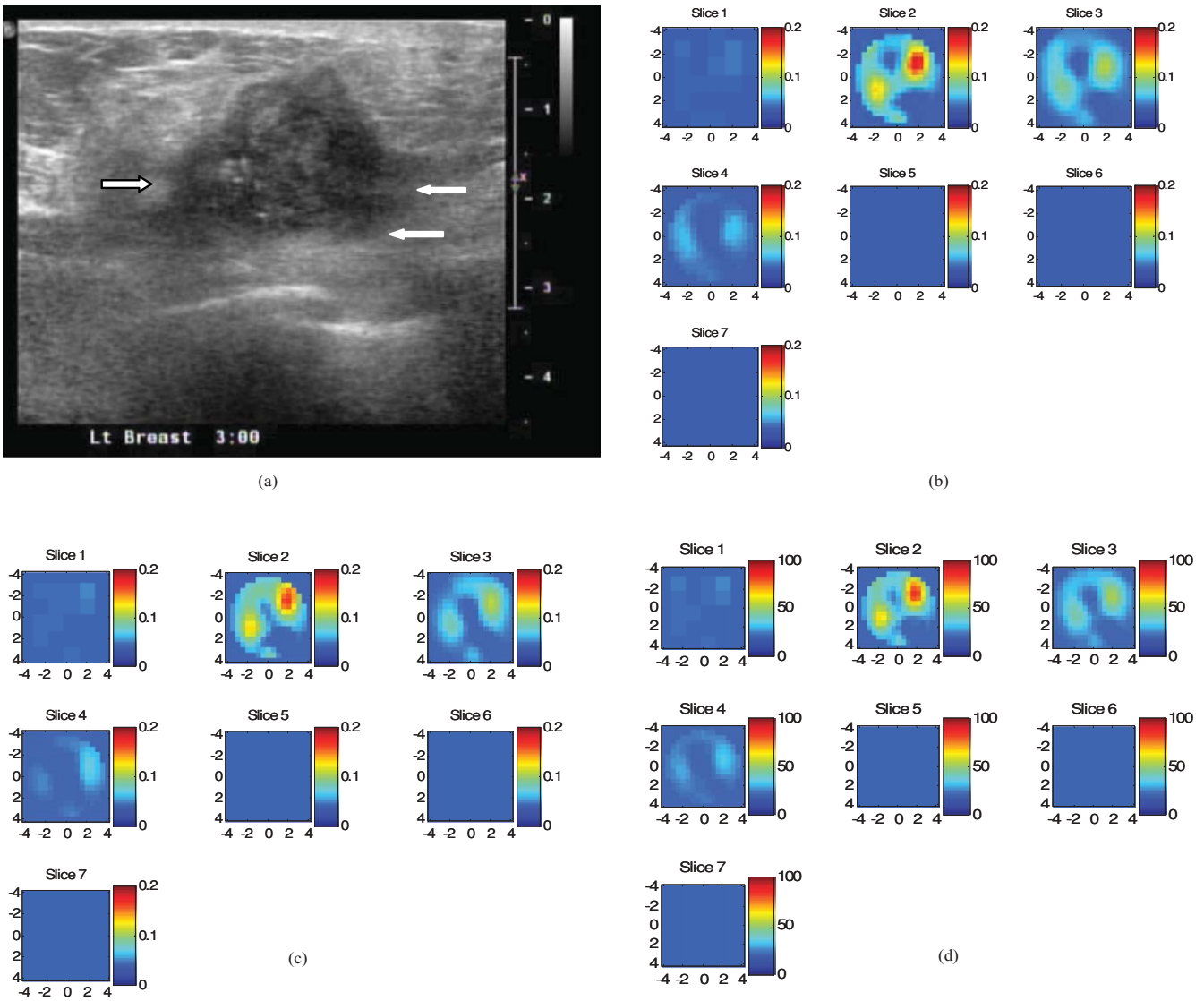

Fig. 21 Clinical example of an advanced cancer: (a) coregistered US showing a suspicious mass of a semispherical shape with top and bottom located at 0.5 and 2.5 cm from the skin surface. A core biopsy revealed a high-grade ductal carcinoma. (b) Optical absorption map reconstructed at 780 nm, (c) absorption map reconstructed at 830 nm, and (d) computed total hemoglobin concentration map.

60% which was lower than that of 70 to 85% obtained from smaller targets.[36,37] The measured contrast of the higher target absorption periphery over the lower absorption core was about a factor of 2 in the best imaging condition. This is due to the intense scattering evens of diffused photons, which causes the information loss between the two groups of photons passing the outer shell only and passing the outer shell and the inner core. Interestingly, several groups have reported the factor of 2 contrast between malignant lesions and background tissues using different instrumentation and different measurement methods.[2,38]

In summary, we showed that large inhomogeneous concentric semiellipsoidal targets with outer shell thicknesses less than 1 cm can be resolved at the typical depth range for breast imaging when reflection geometry is used. For large breast lesions of more than 3 cm in size, the periphery enhancement feature can be used to assist US diagnosis of benign versus malignant lesions.

Acknowledgments

This work has been supported by the National Institute of Health (R01EB002136) and the Donaghue Medical Research Foundation.

References

1. B. J. Tromberg, A. Cerussi, N. Shah, M. Compton, A. Durkin, D. Hsiang, J. Butler, and R. Mehta, "Imaging in breast cancer: diffuse optics in breast cancer: detecting tumors in premenopausal women and monitoring neoadjuvant chemotherapy," *Breast Cancer Res.* **7**(6), 279–285 (2005).
2. D. R. Leff, O. J. Warren, L. C. Enfield, A. Gibson, T. Athanasiou, D. K. Patten, J. Hebden, G. Z. Yang, and A. Darzi, "Diffuse optical imaging of the healthy and diseased breast: a systematic review," *Breast Cancer Res. Treat.* **108**(1), 9–22 (2008).
3. B. Chance, S. Nioka, J. Zhang, E. F. Conant, E. Hwang, S. Briest, S. G. Orel, M. D. Schnall, and B. J. Czerniecki, "Breast cancer detection based on incremental biochemical and physiological properties of breast cancers: a six-year, two-site study," *Acad. Radiol.* **12**, 925–933 (2005).

4. S. P. Poplack, T. D. Tosteson, W. A. Wells, B. W. Pogue, P. M. Meaney, A. Hartov, C. A. Kogel, S. K. Soho, J. J. Gibson, and K. D. Paulsen, "Electromagnetic breast imaging: results of a pilot study in women with abnormal mammograms," *Radiology* **243**, 350–359 (2007).
5. R. Choe, A. Corlu, K. Lee, T. Durduran, S. D. Konecky, M. Grosicka-Koptyra, S. R. Arridge, B. J. Czerniecki, D. L. Fraker, A. Demichele, B. Chance, M. A. Rosen, and A. G. Yodh, "Diffuse optical tomography of breast cancer during neoadjuvant chemotherapy: a case study with comparison to MRI," *Med. Phys.* **32**, 1128–1139 (2005).
6. E. Heffer, V. Pera, O. Schu¨tz, H. Siebold, and S. Fantini, "Near-infrared imaging of the human breast: complementing hemoglobin concentration maps with oxygenation images," *J. Biomed. Opt.* **9**, 1152–1160 (2004).
7. X. Liang, Q. Zhang, C. Li, S. R. Grobmyer, L. L. Fajardo, and H. Jiang, "Phase-contrast diffuse optical tomography1: pilot results in the breast," *Acad. Radiol.* **15**(7), 859–866 (2008).
8. X. Intes, "Time-domain optical mammography SoftScan: initial results," *Acad. Radiol.* **12**(8), 934–947 (2005).
9. L. Spinelli, A. Torricelli, A. Pifferi, P. Taroni, G. Danesini, and R. Cubeddu, "Characterization of female breast lesions from multi-wavelength time-resolved optical mammography," *Phys. Med. Biol.* **50**, 2489–2502 (2005).
10. C. H. Schmitz, D. P. Klemer, R. Hardin, M. S. Katz, Y. Pei, H. L. Graber, M. B. Levin, R. D. Levina, N. A. Franco, W. B. Solomon, and R. L. Barbour, "Design and implementation of dynamic near-infrared optical tomographic imaging instrumentation for simultaneous dual-breast measurements," *Appl. Opt.* **44**, 2140–2153 (2005).
11. A. Athanasiou, D. Vanel, C. Balleyguier, L. Fournier, M. C. Mathieu, S. Delaloge, and C. Dromain, "Dynamic optical breast imaging: a new technique to visualise breast vessels: comparison with breast MRI and preliminary results," *Eur. J. Radiol.* **54**(1), 72–79 (2005).
12. D. Floery, T. H. Helbich, C. C. Riedl, S. Jaromi, M. Weber, S. Leodolter, and M. H. Fuchsjaeger, "Characterization of benign and malignant breast lesions with computed tomographic laser mammography (CTLM)," *Invest. Radiol.* **40**, 328–335 (2005).
13. D. Grosenick, K. T. Moesta, M. Möller, J. Mucke, H. Wabnitz, B. Gebauer, C. Stroszczynski, B. Wassermann, P. M. Schlag, and H. Rinneberg, "Time-domain scanning optical mammography: I. Recording and assessment of mammograms of 154 patients," *Phys. Med. Biol.* **50**(11), 2429–2449 (2005).
14. B. Brooksby, B. W. Pogue, S. Jiang, H. Dehghani, S. Srinivasan, C. Kogel, T. D. Tosteson, J. Weaver, S. P. Poplack, and K. D. Paulsen,"Imaging breast adipose and fibroglandular tissue molecular signatures by using hybrid MRI-guided near-infrared spectral tomography," *Proc. Natl. Acad. Sci. U.S.A.* **103**, 8828–8833 (2006).
15. H. Soliman, A. Gunasekara, M. Rycroft, J. Zubovits, R. Dent, J. Spayne, M. J. Yaffe, and G. J. Czarnota, "Functional imaging using diffuse optical spectroscopy of neoadjuvant chemotherapy response in women with locally advanced breast cancer," *Clin. Cancer Res.* **16**(9), 2605–2614 (2010).
16. Q. Zhang, T. J. Brukilacchio, A. Li, J. J. Stott, T. Chaves, E. Hillman, T. Wu, M. A. Chorlton, E. Rafferty, R. H. Moore, D. B. Kopans, and D. A. Boas, "Coregistered tomographic x-ray and optical breast imaging: initial results," *J. Biomed. Opt.* **10**, 024033 (2005).
17. Q. Zhu, M. Huang, N. Chen, K. Zarfost, B. Jagjivant, M. Kane, P. Hedget, and S. H. Kurtzmant, "Ultrasound-guided optical tomographic imaging of malignant and benign breast lesions: initial clinical results of 19 cases," *Neoplasia* **5**, 379–388 (2003).
18. Q. Zhu, E. B. Cronin, A. A. Currier, H. S. Vine, M. Huang, N. Chen, and C. Xu, "Benign versus malignant breast masses: optical differentiation with US-guided optical imaging reconstruction," *Radiology* **237**, 57–66 (2005).
19. Q. Zhu, S. Tannenbaum, P. Hegde, M. Kane, C. Xu, and S. H. Kurtzman, "Noninvasive monitoring of breast cancer during neoadjuvant chemotherapy using optical tomography with ultrasound localization," *Neoplasia* **10**(10), 1028–1040 (2008).
20. A. Cerussi, D. Hsiang, N. Shah, R. Mehta, A. Durkin, J. Butler, and B. J. Tromberg, "Predicting response to breast cancer neoadjuvant chemotherapy using diffuse optical spectroscopy," *Proc. Natl. Acad. Sci. U.S.A.* **104**, 4014–4019 (2007).
21. S. Jiang, B. Pogue, C. Carpenter, S. Poplack, W. Wells, C. Kogel, J. Forero, L. Muffly, G. Schwartz, K. Paulsen, and P. Kaufman, "Evaluation of breast tumor response to neoadjuvant chemotherapy with tomographic diffuse optical spectroscopy: case studies of tumor region-of-interest changes," *Radiology* **252**, 551–560 (2009).
22. Q. Zhu, P. Hegde, A. Ricci Jr., M. Kane, E. Cronin, Y. Ardeshirpour, C. Xu, A. Aguirre, S. Kurtzman, P. Deckers, and S. Tannenbaum, "early-stage invasive breast cancers: potential role of optical tomography with US localization in assisting diagnosis," *Radiology* **256**(2), 367–378 (2010).
23. D. A. Mankoff, L. K. Dunnwald, J. R. Gralow, G. K. Ellis, A. Charlop, T. J. Lawton, E. K. Schubert, J. Tseng, and R. B. Livingston, "Blood flow and metabolism in locally advanced breast cancer: relationship to response to therapy," *J. Nucl. Med.* **43**(4), 500–509 (2002).
24. J. Folkman, K. Watson, D. Ingber, and D. Hanahan, "Induction of angiogenesis during the transition from hyperplasia to neoplasia," *Nature* **339**, 58–61 (1989).
25. P. Vaupel, F. Kallinowski, and P. Okunieff, "Blood flow, oxygen and nutrient supply, and metabolic microenvironment of human tumors: a review," *Cancer Res.* **49**, 6449–6465 (1989).
26. G. Agrawal, M. Y. Su, O. Nalcioglu, S. A. Feig, and J. H. Chen, "Significance of breast lesion descriptors in the ACR BI-RADS MRI lexicon," *Cancer* **115**(7), 1363–1380 (2009).
27. R. Matsubayashi, Y. Matsuo, G. Edakuni, T. Satoh, O. Tokunaga, and S. Kudo, "Breast masses with peripheral rim enhancement on dynamic contrast-enhanced MR images: correlation of MR findings with histologic features and expression of growth factors," *Radiology* **217**, 841–848 (2000).
28. Q. Zhu, S. H. Kurtzman, P. Hegde, S. Tannenbaum, M. Kane, M. Huang, N. G. Chen, B. Jagjivan, and K. Zarfos, "Utilizing optical tomography with ultrasound localization to image heterogeneous hemoglobin distribution in large breast cancers," *Neoplasia* **7**, 263–270 (2005).
29. C. Xu, B. Yuan, and Q. Zhu, "Optimal probe design for breast imaging using near-infrared diffused light," *J. Biomed. Opt.* **13**(4), 044002:1–10 (2008).
30. C. Xu and Q. Zhu, "Light shadowing effect of large breast lesions imaged by optical tomography in reflection geometry," *J. Biomed. Opt.* **15**(3), 036003 1–16 (2010).
31. Q. Zhu, N. G. Chen, and S. Kurtzman, "Imaging tumor angiogenesis using combined near infrared diffusive light and ultrasound," *Opt. Lett.* **28**(5), 337–339 (2003).
32. G. Spirou, A. Oraevsky, A. Vitkin, and W. Whelan "Optical and acoustic properties at 1064 nm of polyvinyl chloride-plastisol for use as a tissue phantom in biomedical optoacoustics," *Phys. Med. Biol.* **50**, N141–N153 (2005).
33. M. D. Barnes, C.-Y. Kung, N. Lermer, K. Fukui, B. G. Sumpter, and D. W. Noid, "Homogeneous polymer blend microparticles with a tunable refractive index," *Opt. Lett.* **24**(3), 121–123 (1999).
34. A. V. Rajulu, R. L. Reddy, S. M. Raghavendra, and S. A. Ahmed, "Miscibility of PVC/PMMA blend by the ultrasonic and refractive index method," *Eur. Polym. J.* **35**, 1183–1186 (1999).
35. A. T. Stavros, D. I. Thickman, C. L. Rapp, M. A. Dennis, S. H. Parker, and G. A. Sisney, "Solid breast nodules: use of sonography to distinguish between benign and malignant lesions," *Radiology* **196**, 123–134 (1995).
36. Q. Zhu, C. Xu, P. Guo, A. Aguirre, B. Yuan, F. Huang, D. Castilo, J. Gamelin, S. Tannenbaum, M. Kane, P. Hegde, and S. Kurtzman, "Optimal probing of optical contrast of breast lesions of different size located at different depths by US localization," *Technol. Cancer Res. Treat.* **5**(4), 365–380 (2006).
37. C. Xu, B. Yuan, and Q. Zhu, "Optimal probe design for breast imaging using near-infrared diffused light," *J. Biomed. Opt.* **13**(4), 044002 (2008).
38. A. Cerussi, N. Shah, D. Hsiang, A. Durkin, J. Butler, and B. Tromberg, "In vivo absorption, scattering, and physiologic properties of 58 malignant breast tumors determined by broadband diffuse optical spectroscopy," *J. Biomed. Opt.* **11**(4), 044005 (2006).